Fall 12-11-2023

Ultrafast nonlinear dynamics of finite graphene systems

Ahmal Zafar

Ultrafast nonlinear dynamics of finite graphene systems

by

Ahmal Jawad Zafar

Under the Direction of Vadym Apalkov, Ph.D.

A Dissertation Submitted in Partial Fulfillment of the Requirements for the Degree of

Doctor of Philosophy

in the College of Arts and Sciences

Georgia State University

2023

ABSTRACT

We study theoretically nonlinear dynamics of a graphene nanoflake placed in the field of an ultrashort optical pulse. We describe the graphene system within an effective model with infinite mass boundary conditions. For an optical pulse with a duration of just a few femtoseconds, the electron dynamics is coherent and is described by a time-dependent Schrödinger equation. For graphene nanoring, if the optical pulse is circularly polarized, then two valleys of graphene are populated differently, resulting in a finite valley polarization of the system after the pulse. Such valley polarization is a unique property of graphene nanoscale systems, while for a graphene monolayer, a circularly polarized pulse does not produce any valley polarization. The valley polarization of a graphene nanoring depends on the parameters of the system, such as inner and outer radii. With the system's size increasing, the valley polarization monotonically decreases, converging to its zero value for the infinite graphene monolayer. Furthermore, we theoretically study the generation of high harmonics in disk shape graphene quantum dots placed in (i) linearly and (ii) and subsequently, a transition to circularly polarized short pulses. The length gauge was used to describe the interaction of quantum dots with an optical pulse. The generated radiation spectra of graphene quantum dots as a result of a linearly polarized pulse can be controlled by varying the quantum dot size, i.e., its radius. With increasing the quantum dot radius, the intensities of low harmonics mainly decrease, while the cutoff frequency increases. The sensitivity of the cutoff frequency to the QD size increases with the intensity of the pulse. Moreover, the transition from linearly to circularly polarized pulse suppresses the harmonics and cutoff frequency in radiation spectra. The cutoff frequency is independent of the size of a quantum dot when a completely circularly polarized pulse is shined. The cutoff frequency and intensity of harmonics can be tuned by the ellipticity and frequency of the laser pulse.

INDEX WORDS: Ultrafast Process, Graphene Quantum Dots (QDs), Valleytronics, High Harmonic Generation (HHG), Non-linear electron dynamics, Broken time-reversal symmetry.

Ultrafast nonlinear dynamics of finite graphene systems

by

Ahmal Jawad Zafar

Committee Chair: Vadym Apalkov

Committee: Brian D. Thoms

Sidong Lei

Electronic Version Approved:

Office of Graduate Services

College of Arts and Sciences

Georgia State University

December 2023

DEDICATION

To my beloved mother.

ACKNOWLEDGMENTS

I wish to express my profound gratitude to Dr. Vadym Apalkov, my advisor and the chair of my Ph.D. committee. His unwavering guidance, ceaseless support, and invaluable opportunities enriched my journey. The experience under his mentorship was truly enriching, characterized by boundless support and enlightening discussions.

I am equally thankful to my committee members: Dr. Brian D. Thoms, and Dr. Sidong Lei for their insightful feedback and time dedicated to evaluating my dissertation.

A heartfelt appreciation goes to my friends Aranyo Mitra, Rezvan Husseini, and Dr. Aisha Okmi. Their unwavering belief in me and their support during challenging times have been invaluable.

Expressing my deepest gratitude to the distinguished professors and mentors at Quaid-i-Azam University, Islamabad, is paramount, for their guidance has been instrumental in shaping my academic trajectory.

I extend my profound gratitude to the esteemed faculty, dedicated staff, and distinguished peers of Georgia State University for their instrumental contributions to my intellectual and personal maturation throughout my tenure. Their unwavering support, encouragement, and insightful guidance have been indispensable in facilitating my attainment of this significant academic milestone.

To my family, whose support forms the bedrock of my achievements, I owe more than words can express. My siblings, always my pillars of strength, have consistently believed in

and stood by me.

Lastly, I'd like to extend my gratitude to my Postdoc mentor, Dr. S. Azar Oliaei Motlagh, for her invaluable assistance and support.

TABLE OF CONTENTS

ACKNOWLEDGMENTS . . . . . **v**

LIST OF FIGURES . . . . . **ix**

1 Introduction **1**

1.1 Ultrafast Lasers 1

1.2 Graphene Monolayer 2

1.3 Graphene Nanoflake 5

2 METHODOLOGY **7**

2.1 Effective Model 7

2.2 Roots of Eigenvalue Equation 11

2.3 Numerical method to solve TDSC 12

2.4 Fourier Transformation 14

3 Ultrafast Valley Polarization **17**

3.1 Introduction 17

3.2 Eigenvalue Equation 18

3.3 Results and Discussion 19

3.4 Conclusion 36

4 High Harmonic Generation by Linearly Polarized Laser Pulse **38**

4.1 Introduction 38

4.2 Energy Spectrum 40

4.3 Results and Discussion 43

4.4 Conclusion 50

5 Generation of High Harmonics in a Graphene Quantum Dot Exhibiting Broken Time-Reversal Symmetry 51

5.1 Introduction 51

5.2 Results and Discussion 53

6 SUMMARY 65

Appendices 68

A Appendix A 69

B Appendix B 88

REFERENCES 95

LIST OF FIGURES

Figure 1.1 (a) The hexagonal honeycomb lattice characteristic of graphene comprises two interpenetrating triangular sublattices, denoted as A (illustrated by the black circle) and B (depicted by the white circle). (b) Within the first Brillouin zone of this honeycomb lattice, two distinct valleys, labeled K and K', are positioned along its perimeter. (c) The energy dispersion for graphene within the extended zone. The delineated black lines demarcate the boundaries of the primary Brillouin zone. [1] 3

Figure 1.2 Illustration of Graphene Nanoflake of a triangular shape. The number of atoms is mentioned in each panel. [2] 6

Figure 3.1 Schematic diagram of Graphene Quantum Ring. 18

Figure 3.2 Energy spectra of graphene nanoring. The spectra are shown as a function of magnetic quantum number m, which takes half-integer values. The size of the nanoring is $R_{\text{in}} = 5$ nm, $R_{\text{out}} = 15$ nm in panels (a) and (b); $R_{\text{in}} = 5$ nm, $R_{\text{out}} = 35$ nm in panels (c) and (d). The spectra are shown for the K valley [panels (a) and (c)] and for the K' valley [panels (c) and (d)]. 21

Figure 3.3 Profile of the electric field of a left circularly polarized optical pulse. The pulse has only one oscillation. The amplitude of the pulse is $F_0 = 0.1$ V/Å. The optical field has both x and y components. The inset shows the corresponding one cycle of the optical pulse. 24

Figure 3.4 Conduction band population as a function of time. The conduction band states are the states with positive energies. The data are shown for different field amplitudes for the K valley [panel (a)] and the K' valley [panel (b)]. The corresponding values of F_0 are shown next to each line. The inner and outer radii of the nanoring are $R_{\text{in}} = 5$ nm, $R_{\text{out}} = 15$ nm. The time constant, which determines the frequency and the duration of the optical pulse, is $\tau = 1$ fs. The optical pulse is left circularly polarized. 26

Figure 3.5 Conduction band population as a function of time. The conduction band states are the states with positive energy. The data are shown for different value of parameter τ for the K valley [panel (a)] and the K' valley [panel (b)]. The corresponding values of τ are shown next to each line. Parameter τ determines both the frequency of the pulse and its duration. The time is shown in dimensionless units, t/τ. The inner and the outer radii of the nanoring are $R_{\text{in}} = 5$ nm and $R_{\text{out}} = 15$ nm. The field amplitude is $F_0 = 0.1$ V/Å. The optical pulse is left circularly polarized. 27

Figure 3.6 Population of individual conduction band levels. The results are for the K valley [panels (a), (b), and (c)] and the K' valley [panels (d), (e), and (f)]. The amplitude of the pulse is $F_0 = 0.1$ V/Å[panels (a) and (d)], $F_0 = 0.2$ V/Å[panels (b) and (e)], $F_0 = 0.3$ V/Å[panels (c) and (f)]. The inner and the outer radii of the nanoring are $R_{\text{in}} = 5$ nm and $R_{\text{out}} = 15$ nm. The red lines correspond to in-gap edge states, while the blue lines correspond to bulk states of the nanoring. The time constant of the pulse is $\tau = 1$ fs. The optical pulse is left circularly polarized. 28

Figure 3.7 Population of individual conduction band levels. The results are for the K valley [panels (a) and (b)] and the K' valley [panels (c) and (d)]. The time constant of the optical pulse is $\tau = 1$ fs [panels (a) and (c)] and $\tau = 2$ fs [panels (b) and (d)]. The inner and the outer radii of the nanoring are $R_{\text{in}} = 5$ nm and $R_{\text{out}} = 15$ nm. The red lines correspond to in-gap edge states, while the blue lines correspond to bulk states of the nanoring. The amplitude of the pulse is $F_0 = 0.1$ V/Å. The optical pulse is left circularly polarized. . . . 29

Figure 3.8 The valley polarization of a graphene nanoring. The valley polarization is defined by Eq. (2.9) and is shown as a function of the field amplitude F_0 for different parameters of the nanoring. In panel (a), the inner radius is fixed at $R_{\text{in}} = 5$ nm and the outer radius is varied with the corresponding values shown next to each line. In panel (b), the outer radius is fixed at $R_{\text{out}} = 35$ nm, and the inner radius is varied with the corresponding values shown next to each line. The time constant of the pulse is $\tau = 1$ fs, and the pulse is left circularly polarized. The insets in each panel show the valley polarization at small values of F_0. 31

Figure 3.9 The valley polarization of a graphene nanoring. The valley polarization is defined by Eq. (2.10) and is shown as a function of the field amplitude F_0 for different parameters of the nanoring. In panel (a), the outer radius is fixed at $R_{\text{out}} = 35$ nm, and the inner radius is varied with the corresponding values shown next to each line. In panel (b), the inner radius is fixed at $R_{\text{in}} = 5$ nm, and the outer radius is varied with the corresponding values shown next to each line. The time constant of the pulse is $\tau = 1$ fs, and the pulse is left circularly polarized. 33

Figure 3.10 The valley polarization of a graphene nanoring. The valley polarization is defined by Eq. (2.10) and is shown as a function of the field amplitude F_0 for different parameters of the nanoring. In panel (a), the outer radius is fixed at $R_{\text{out}} = 35$ nm, and the inner radius is varied with the corresponding values shown next to each line. In panel (b), the inner radius is fixed at $R_{\text{in}} = 5$ nm, and the outer radius is varied with the corresponding values shown next to each line. The time constant of the pulse is $\tau = 1$ fs, and the pulse is left circularly polarized. 35

Figure 4.1 Schematic Representation of a Graphene Quantum Disk Interacting with an x-Polarized Laser Pulse 40

Figure 4.2 Energy spectra of graphene quantum dots. The energy spectra are shown for the K (a), (d) and K' (c), (d) valleys. The radius of the quantum dot is 15 nm (a), (c) and 30 nm (b), (d). 42

Figure 4.3 Profile of the electric field of the pulse as a function of time. The amplitude of the pulse is 0.2 V/Å. The frequency of the pulse is 1 rad/fs and the pulse duration is determined by parameter $\tau = 15fs$. 44

Figure 4.4 Radiation spectra of graphene quantum dots. The frequency and the amplitude of the pulse are marked in each panel. Different lines in each panel correspond to different radii of graphene quantum dots. The intensities are shown in the logarithmic scale and the frequency is shown in units of the frequency of the pulse, ω_0. 45

Figure 4.5 Intensities of high harmonics as a function of quantum dot radius. The data are shown for the first three harmonics: the third harmonic (a), (d), (g); the fifth harmonic (b), (e), (h); the seventh harmonic (c), (f), (i). The frequency of the pulse is marked in each panel. Different lines in each panel correspond to different pulse amplitudes, which are shown next to the corresponding lines. 47

Figure 4.6 High harmonic cutoff as a function of the quantum dot radius. The frequency of the pulse is 1 rad/fs (a), 0.5 rad/fs (b, and 0.25 rad/fs (c). Different lines in each panel correspond to different field amplitudes, which are marked next to the corresponding lines. 49

Figure 5.1 Schematic Representation of a Graphene Quantum Disk Interacting with Circulalry polarized Light and the Dipole moment as a result of interaction between QD and Ultrafast Pulse. 51

Figure 5.2 Radiation spectra of graphene QD. The frequency and size of QD are mentioned in each panel. Each line of the panel corresponds to a different ellipticity of the incident laser pulse. The vertical axis shows the intensities on a logarithmic scale, and frequencies are shown in units of frequency of the incident pulse. 54

Figure 5.3 Intensities of (a) third and (b) fifth harmonics as a function of ellipticity α for three radii studied. The frequency of the applied pulse is mentioned in the panels. 56

Figure 5.4 Ellipticity of Dipole moment at the third and fifth harmonic peak as a function of ellipticity of applied pulse. The radius of the QD and frequency of the applied pulse are mentioned in the plot. 59

Figure 5.5 Schematic Diagram of an elliptically polarized ultrafast laser pulse and the resultant Elliptically Polarized Dipole moment in an opposite direction between the range $\alpha = 0.2 - 0.75$. 60

Figure 5.6 High Harmonic cutoff as a function of ellipticity α of the applied pulse. Two lines in the panel correspond to ω_0 0.5 rad/fs and 1 rad/fs. 61

Figure 5.7 The cutoff frequency as a function of ellipticity parameter (α). Each line within the panel represents distinct radius values of the quantum dot (QD). The frequency of the applied pulse is denoted within the panel 63

CHAPTER 1
Introduction

1.1 Ultrafast Lasers

Efforts to develop a method for measuring the briefest interval of time have been long standing in the scientific arena [3]. Lasers with femtosecond pulse duration were developed forty years ago and it has dominated the field for over the last couple of decades [4]. The development of femtosecond ($1fs = 10^{-15}s$) Laser allowed the direct-domain research of immeasurably fast processes such as phase transitions, structural dynamics of molecules, and chemical reactions in condensed matter physics [5, 6]. Basically, at an ultrafast timescale, all types of structural dynamics are static, allowing a pump-probe spectroscopy in real-time observation for electronic phenomena in solids [7]. Subsequently, a single-cycle pulse of ultrashort duration is ultimately paramount to investigating the nonperturbative strong-field interactions, where electron dynamics change within a fraction of the optical cycle [8].

The development of theoretical models to study the strong-field interaction in solids requires an understanding of how a solid behaves in an external electric field. An external field with an intensity of the order of 1 V/Å, can result in irreversible electron dynamics in the materials with a small bandgap, i.e. the conduction band has persistent nonzero electron population after the pulse [9]. The study of nanoscale systems interacting with an ultrafast pulse has been extensively studied over the last few decades. Notably, the 2023 Nobel Prize was awarded for the advancement in the study of ultrashort electron dynamics [10]. The interest in these systems is related to their unique transport, optical, and topological

properties. The interaction of ultrafast laser with nanodevices can cause irreversible and nonadiabatic transitions of electron population from valance band to conduction band, that can sustain even after the pulse. The results of these irreversible dynamics can result in many nontrivial and interesting properties which can have various applications [11, 12].

1.2 Graphene Monolayer

A graphene monolayer is a single layer of carbon atoms which form a honeycomb crystal structure with two inequivalent sublattices, say, A and B. One of the unique features of the graphene monolayer is its low-energy relativistic dispersion of a Dirac type [11].

The corresponding electron states are chiral, where the chirality is related to the pseudospin originating from the two graphene sublattices. The chiral nature of electron states brings such unique effects as Klein tunneling, strong suppression of backscattering, and localization [13].

Another attractive property of the graphene monolayer is the existence of two valleys in its reciprocal space. The valleys are located at the K and K' points at the vertices of the hexagonal first Brillouin zone of graphene and follow a linear dispersion. [14], see Fig. 1.2

$$E = \hbar v_F k. \tag{1.1}$$

The energy spectra at these points are gapless and relativistic; that is, they are the Dirac points. The time-reversal operator connects the K and K' valleys. Here, the time-reversal symmetry is the symmetry of the graphene monolayer. Electrons in graphene also have

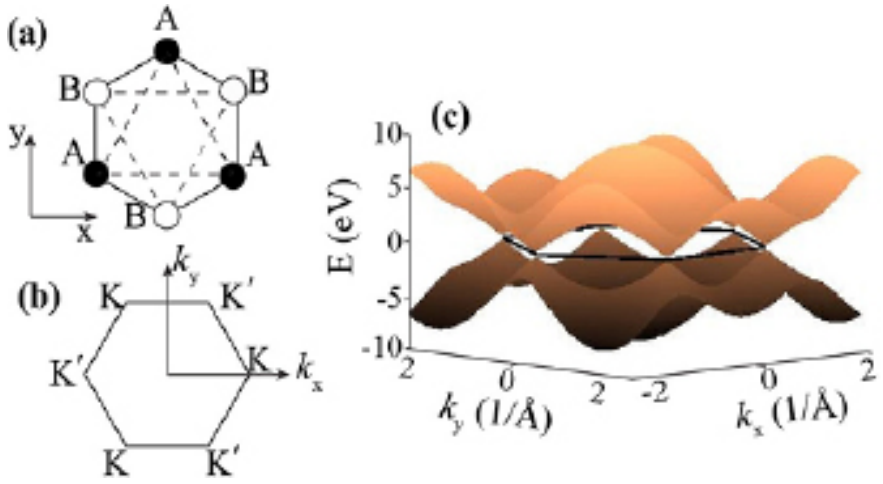

Figure 1.1 (a) The hexagonal honeycomb lattice characteristic of graphene comprises two interpenetrating triangular sublattices, denoted as A (illustrated by the black circle) and B (depicted by the white circle). (b) Within the first Brillouin zone of this honeycomb lattice, two distinct valleys, labeled K and K', are positioned along its perimeter. (c) The energy dispersion for graphene within the extended zone. The delineated black lines demarcate the boundaries of the primary Brillouin zone. [1]

nontrivial local topological properties. Namely, while the net topological charge (Chern number) for the whole Brillouin zone of graphene is zero, and the topological charges at the K and K' points are 1 and -1, respectively [15].

The existence of the two valleys in graphene opens a possible application of graphene in valleytronics [16, 17, 18], where the valley degree of freedom can be used for information storage and quantum computer applications. The two valleys in graphene are well separated in the reciprocal space, and an intervalley scattering is strongly suppressed for a smooth scattering potential. In this relation, there is a problem with how to generate and manipulate valley polarization in graphene. Here, in this study, the valley polarization is determined by the different valley populations of the system. To generate the valley polarization in graphene, the time-reversal symmetry should be broken. This can be done, for example, by

an incident circularly polarized pulse. If such a pulse is ultrashort with just a few oscillations of the field, then it will allow controlling the valley degree of freedom on the femtosecond timescale. In Refs. [19, 20, 21], interactions of graphene-like systems with a circularly polarized short and ultrastrong pulse were considered. It was found that such a pulse can induce large final valley polarization, but to have such a valley polarization, the inversion symmetry of graphene should be broken. This means that graphene should have a finite band gap. Under such a condition, the valley polarization is generated due to the effect of topological resonance [20, 21, 22]. The topological resonance is a cancellation of a dynamic phase by a topological phase, which is accumulated during a strong optical pulse. In pristine graphene that has a zero band gap, the topological phase, which consists of a geometric phase (Berry phase) and a phase of an interband dipole matrix element (non-Abelian Berry connection), is effectively zero, so no topological resonance can be observed in such a system. In graphene systems with broken inversion symmetry, the topological phase is proportional to the band gap and has different signs at the two valleys, which results in the valley-dependent topological resonance [22]. The inversion symmetry is broken in graphene-like materials with two sublattices occupied by different atoms, e.g., transition-metal dichalcogenides (TMDCs) [23, 24, 25], and in silicene/germanene, which has a buckled hexagonal shape and in which the perpendicular electric field breaks the inversion symmetry [26, 27, 28]. In graphene, a small band gap can also be opened if it is placed on different types of substrates, e.g., on SiC [29, 30]. The finite valley polarization of TMDC monolayers placed in an ultrashort circularly polarized pulse was predicted theoretically in Ref. [20] [13].

1.3 Graphene Nanoflake

In this study, we propose another method to generate ultrafast non-linear dynamics in graphene materials. We consider a nanoflake of graphene. An example of such a system is a graphene quantum dot (QD) [31, 32, 33]. For such a system, a translational symmetry is broken and the bandgap is opened due to a dimensional quantization. Quantum dots and other types of nanosize systems are zero-dimensional, i.e., electrons are confined in all spatial directions and occupy spectrally sharp energy levels like those found in atoms [34, 35, 36]. Similar to conventional atoms, the properties of QDs, which are also called artificial atoms, are governed by the Hund's rule [36, 37], which determines electron occupations of degenerate QD energy levels, the Coulomb blockade [38], which is a manifestation of electron-electron interactions within the QD, and the Kondo effect [39], which is related to electron spin.

The QDs are between a few nanometers to a few microns in size. Due to such a tiny scale, the QDs can be occupied by just a few electrons, which allows controlling and optimizing QD-based nanoscale devices. The QDs also show superior transport and optical properties with many applications in different fields of science, such as semiconductor lasers [40], quantum computers [41], biomedical systems [42], light-energy conversion [43, 44].

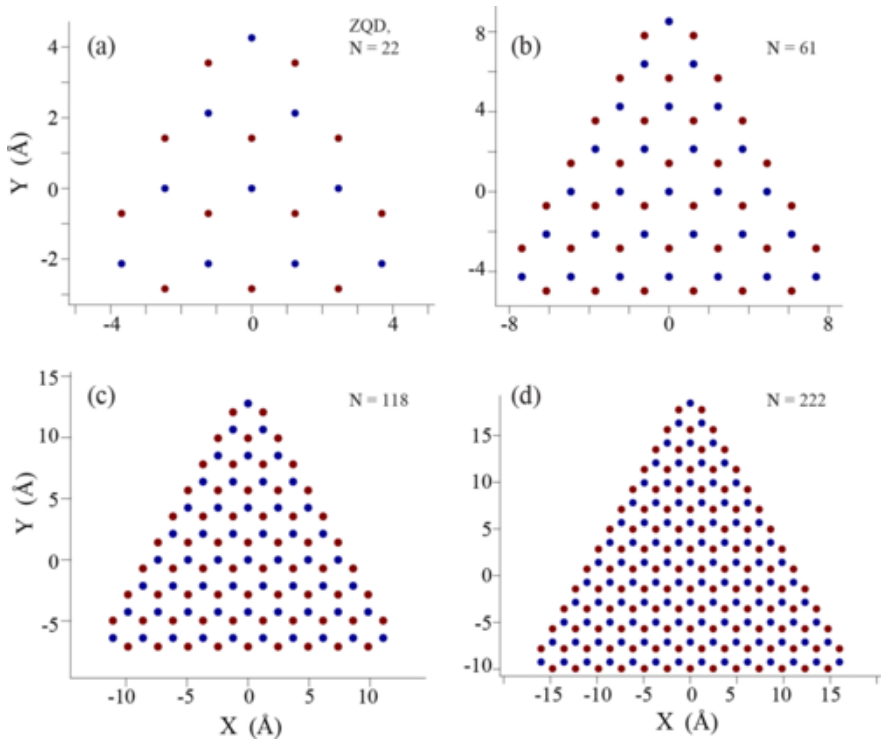

Figure 1.2 Illustration of Graphene Nanoflake of a triangular shape. The number of atoms is mentioned in each panel. [2]

CHAPTER 2
METHODOLOGY

2.1 Effective Model

This chapter will establish the mathematical foundations of ultrafast optical response in low-dimensional materials. We describe graphene within an effective low-energy model with the Hamiltonian of a Dirac type, which for graphene quantum dot takes the following form

$$\mathcal{H}_0^{(\xi)} = \frac{\gamma}{\hbar}(\sigma_x p_x + \xi \sigma_y p_y) + V(\mathbf{r}), \tag{2.1}$$

where σ_x and σ_y are the Pauli matrices, $p_x = -i\hbar\nabla_x$, $p_y = -i\hbar\nabla_y$, $\gamma = \sqrt{3}a_0\gamma_0/2$ is the band parameter with the lattice constant $a_0 = 0.142$ nm and the nearest neighbor hopping integral $\gamma_0 = 3.03$ eV. Here ξ is the valley parameter, which is +1 for the K valley and -1 for the K' valley. Since the spin-orbit interaction is very weak in graphene, the Hamiltonian (2.1) is written only for one spin component, e.g., spin up. Thus, each energy level calculated below has an extra double spin degeneracy.

The Hamiltonian $\mathcal{H}_0^{(\xi)}$ carries the information of low energy electrons confined in an external potential $V(\mathbf{r})$ which is of the form $V(\mathbf{r}) = \Delta(\mathbf{r})\sigma_z$, where σ_z is the Pauli matrix. Here $\Delta(\mathbf{r})$ is zero inside quantum dot and $\Delta(r) \to \infty$ outside. Such a profile of the confinement potential introduces infinite mass boundary conditions [45, 46, 47, 48] at the boundary of the nanoring. Although the properties of graphene quantum dot depends on the type of their edges, e.g., zigzag or armchair edges, the infinite boundary conditions can be a good approximation for graphene nanostructures that are etched out of graphene sheets by lithography,

see Ref. [48, 49, 50, 51, 52].

We apply the Ultrafast Laser pulse on a graphene quantum dot, which is of the shape of Disk and Ring, to analyze its response in femtosecond time intervals. The electron dynamics of the finite Graphene system under the influence of an external field is described by the time-dependent Schrodinger equation.

$$i\hbar\frac{d\Psi^{(\xi)}(t)}{dt} = \mathcal{H}^{(\xi)}(t)\Psi^{(\xi)}(t). \tag{2.2}$$

In the presence of such a short and intense pulse, the interaction term of the field with matter is governed by length gauge or dipole approximation.

$$\mathcal{H}^{'}(t) = e\mathbf{F}(t)\cdot\mathbf{r}, \tag{2.3}$$

where $\mathbf{F}(t)$ is the pulse's electric field. The complete Hamiltonian of the system that describes its time evolution is given by;

$$\mathcal{H}^{(\xi)}(t) = \mathcal{H}_0^{(\xi)} + e\mathbf{F}(t)\cdot\mathbf{r}, \tag{2.4}$$

We expand a solution of Eq. (2.2) in the basis of single-particle states , ψ_i,

$$\Psi^{(\xi)}(t) = \sum_{j=1}^{N}\beta_j^{(\xi)}(t)\psi_i^{(\xi)}e^{-\frac{i}{\hbar}E_j t}, \tag{2.5}$$

With the time-dependent expansion coefficients $\beta_i^{(\xi)}(t)$. Strictly speaking, the energy spectrum of the graphene finite systems, within the effective low energy model, consists of an

infinite number of levels, both in the conduction and valence bands. In our approach, we consider a finite number N of Energy levels, the energies of which are in the interval from -2 eV to 2 eV. The number of such levels depends on the size of the system.

The intensity of the optical pulse we consider below is small enough, so the pulse's electric field does not mixture the states of different valleys. The amplitude of the pulse, which can result in the coupling of the valleys, can be estimated from the condition that, during the pulse, an electron is transferred between the two valleys, i.e., over the distance of $4\pi/3\sqrt{3}a_0$. The corresponding field amplitude can be estimated as $F_0 \approx 4\pi\hbar/3\sqrt{3}\tau a_0 \approx 1.1$ V/Å. Below, we consider the optical pulses with amplitudes less than 0.5 V/Å. The coefficients $\beta_i(t)$ in Eq. (3.14) satisfy the following system of differential equations

$$\frac{d\beta_k^{(\xi)}}{dt} = -\frac{i}{\hbar}\sum_{j=1}^{N}\mathbf{F}(t)\cdot\mathbf{D}_{kj}^{(\xi)}(t)\beta_j^{(\xi)}e^{-\frac{i}{\hbar}(E_j-E_k)t}. \tag{2.6}$$

With the known wavefunctions, the dipole matrix elements between the states i and j can be calculated from the following expression

$$\mathbf{D}_{ij}^{(\xi)} = \left\langle \psi_j^{(\xi)}|e\mathbf{r}|\psi_i^{(\xi)}\right\rangle. \tag{2.7}$$

We solve the system of equations (2.6) numerically with the conditions that all the valence band (VB) states are initially occupied, and all the conduction band (CB) states are empty. The equations are solved by the Runge-Kutta method, where the initial time is -3τ and the final time is 3τ. From the solution of Eq. (2.6) we obtain the final populations of the CB levels, i.e., the populations after the pulse. We find the CB populations for both the K and

K' valleys,

$$\mathcal{N}_{CB}^{(\xi)}(t) = \sum_{j\in \mathrm{CB}} \left|\beta_j^{(\xi)}(t)\right|^2. \tag{2.8}$$

Then, we define the final valley polarization of the graphene nanoring. To better characterize the asymmetry in valley populations of the system, we introduce two different expressions for the valley polarization. In the first expression, the valley polarization is defined as the difference between the CB populations of different valleys,

$$P = \frac{\mathcal{N}_{CB}^{(K)}(t=\infty) - \mathcal{N}_{CB}^{(K')}(t=\infty)}{Area}, \tag{2.9}$$

where the valley polarization is defined per unit area of the nanoring. The second expression defines the normalized valley polarization,

$$P_N = \frac{\mathcal{N}_{CB}^{(K)}(t=\infty) - \mathcal{N}_{CB}^{(K')}(t=\infty)}{\mathcal{N}_{CB}^{(K)}(t=\infty) + \mathcal{N}_{CB}^{(K')}(t=\infty)}. \tag{2.10}$$

This expression determines the fraction of the excited electrons, which occupy the two valleys differently. The maximum value of P_N is one, corresponding to the condition that all electrons are excited in one valley only.

With the known solutions $\beta_{n,i}^{(\xi)}(t)$ for all values of n, where n belongs to the valence band, we can find the time-dependent dipole moment of the system from the following expression

$$d_x(t) = \sum_{\xi} \sum_{n\in \mathrm{VB}} \sum_{i,j} \beta_{n,i}^{(\xi)*}(t)\beta_{n,j}^{(\xi)}(t) D_{x,ij}^{(\xi)} e^{\frac{i}{\hbar}(E_j - E_i)t}, \tag{2.11}$$

where the sum over n is over the valence band states and $D_{x,ij}^{(\xi)}$ is the dipole matrix element defined in Eq. (2.7).

The time variation of the dipole moment determines the radiation of the system. At

a given frequency ω, the intensity of the corresponding radiation is given by the following expression

$$I(\omega) = \frac{\mu_0 \omega^2}{12\pi c} |\mathcal{F}_\omega[\dot{d}_x]|^2, \tag{2.12}$$

where $\mathcal{F}_\omega[\dot{d}_x]$ is the frequency Fourier transform of the time derivatives of the dipole moment. The order of the generated high harmonic is defined in units of ω_0, i.e.,

$$N_\omega = \frac{\omega}{\omega_0}. \tag{2.13}$$

2.2 Roots of Eigenvalue Equation

A finite Graphene system solved by using the Dirac Effective model, unfortunately, does not derive the analytical expression to find the Eigenvalues of the system, i.e., the energy levels. A modified bisection method is implemented as a root-finding algorithm that divides the total interval Egenvalue output into two sub-intervals and then selects the sub-interval in which a root must lie. This method is applied iteratively until the width of the sub-interval is reduced to the desired precision.

The proposed algorithm is meticulously constructed to iteratively evaluate all plausible values of the eigenvalue equation, pinpointing locations where the function either intersects the x-axis or undergoes a sign change. An interval $[a, b]$ is selected, grounded on estimations commonly derived from the Gershgorin circle theorem or other analogous methods. For each identified point, the algorithm determines the average of the two bounding values, considering it as a potential solution to the eigenvalue equation. The midpoint of the interval

is computed as $(a + b)/2$. If there's a sign change in the values of the eigenvalue equation within the interval, the algorithm registers that point and proceeds to the subsequent interval. Employing this approach, the algorithm passes over a predefined set of values to catalog all zero-crossings, which correspond to solutions of the eigenvalue equation.

A notable challenge in selective solutions for a finite graphene system with two boundaries is the potential misidentification of zero crossings resulting from the equation's asymptotic behavior, rather than genuine solutions. To address this, we integrated a filtration mechanism that detects points characterized by the function's asymptotic tendencies. Subsequent to this identification, these points are excluded from the previously saved zero-crossings, ensuring only solutions of genuine physical relevance are retained. See Listing 1 in Appendix A for the MATLAB code.

However, it is noted that the eigenvalue equation for a finite graphene system with one boundary, which is a Quantum Disk does not possess asymptotic solutions, the implementation of the algorithm was straightforward.

2.3 Numerical method to solve TDSC

The electron dynamics and optical response of a finite Graphene system require solutions of time dependent differential equation mentioned above, Eq. 2.6. As each energy level is coupled with all other energy levels of the spectrum directly or indirectly because of selection rules governed by Dipole matrix elements, Eq. 2.7. This means there are as many coupled differential equations as the number of energy levels. For the system with the largest

dimension selected in this study, the total number of energy levels are more than 200, which mean there are the same amount of coupled differential equation that needs to be solved simultaneously over the time interval of the laser pulse to study the electron dynamics on the entire time range.

Sophisticated numerical techniques exist for resolving first-order differential equations. These methods broadly fall into two categories: linear multistep methods and Runge-Kutta techniques. The linear multistep category encompasses the Adams-Moulton method, and the backward differentiation method (BDF). On the other hand, Runge-Kutta techniques feature methods such as the standard fourth-order technique, Forwarded Euler approach, Heun's method, Fehlberg RK1 method, and the Dormand-Prince method.

Typically, Runge-Kutta techniques involve multiple evaluations of $f(t, y)$ to enhance precision. An archetype of a standard 4th-order Runge-Kutta method is given by [53, 54, 55]:

$$y_{n+1} = y_n + h\left(\frac{K_0}{6} + \frac{K_1 + K_2}{3} + \frac{K_3}{6}\right)$$

Where:

$$K_0 = f(t_n, y_n)$$
$$K_1 = f\left(t_n + \frac{h}{2}, y_n + \frac{h}{2}K_0\right)$$
$$K_2 = f\left(t_n + \frac{h}{2}, y_n + \frac{h}{2}K_1\right)$$
$$K_3 = f(t_n + h, y_n + hK_2)$$

Here, h represents the step size. It's a common practice to utilize Runge-Kutta techniques in tandem, pairing a lower-order with a higher-order method for the same progression. For the numerical evaluation of we employ the ode45 solver from MATLAB, a tool that is a top recommendation for such computations.

Parallel Processing Modules, In computational mathematics and high-performance simulations, MATLAB has positioned itself as a standard tool, offering many functionalities to researchers. Among its numerous toolboxes, the Parallel Computing Toolbox stands out, especially when dealing with large datasets or computationally intensive tasks. This toolbox introduces the powerful **"parfor"** loop, a parallelized version of the standard **"for"** loop, which has been designed to distribute iterations across multiple cores or even computational nodes.

As previously discussed, to solve over 200 coupled differential equations simultaneously by using the Runge-Kutta technique, we employed MATLAB's parallel processing capabilities in conjunction with a Linux-based high-performance computing system. This approach facilitated the computation of $\beta_{n,i}^{(\xi)}(t)$, representing the transition probability of electrons in response to a time-dependent field.

2.4 Fourier Transformation

Named after the French mathematician Jean-Baptiste Joseph Fourier, this transformation reveals the frequency components present within a time-domain signal, providing a decomposition of the signal in terms of sinusoids of different frequencies. Mathematically, the Fourier

Transform of a continuous function $f(t)$ is defined as:

$$F(f) = \int_{-\infty}^{\infty} f(t) e^{-j2\pi ft}\, dt$$

Where $F(f)$ represents the complex amplitude of the frequency component at frequency f, and j is the imaginary unit.

As mentioned in Eq. 2.12, we require the Fourier transformation of the time derivative of the dipole moment. Since the Dipole moment is in the time domain, its Fourier transformation in the frequency domain gives us the emission spectrum of Quantum Dot, and the detailed spectrum of High-Harmonics generated as a result of Ultrafast laser Pulse.

We used MATLAB's fft function to compute the discrete Fourier transform (DFT) of dipole moment, which is a sampled version of the continuous Fourier transform. The function $Y = \text{fft}(X)$ in MATLAB corresponds to the Fourier transform. Given sequences X and Y of length n, the algorithm for these transforms are mathematically represented as [56]:

$$Y(k) = \sum_{j=1}^{n} X(j) W_n^{(j-1)(k-1)} \Delta j$$

and

$$X(j) = \frac{1}{n} \sum_{k=1}^{n} Y(k) W_n^{-(j-1)(k-1)} \Delta k$$

where

$$W_n = e^{-\frac{2\pi i}{n}}$$

denotes one of the n roots of unity. The fft function essentially provides a numerical approximation to this integral for discretely sampled signals, thereby offering insights into the frequency components of the sampled input data. See Listing 2 in Appendix 2 for the MATLAB code.

CHAPTER 3

Ultrafast Valley Polarization

3.1 Introduction

In this Chapter, we consider graphene nanosize systems of a special shape. Namely, we consider graphene nanorings, Fig 3.1. Similar to QDs, nanorings have discrete energy spectra with unique transport and optical properties. Graphene nanorings have two parameters, the inner and outer radii of the ring, which can be used to tune their properties. Below, to describe an electron system of graphene nanoring, we use an effective model, which is applied separately to the K and K' valleys of graphene. Interaction of the graphene nanoring with an ultrashort circularly polarized optical pulse should generate different conduction band populations of the two valleys, resulting in finite final valley polarization of the system.

Because the nanoring has cylindrical symmetry, its electron states are characterized by a z-component of angular momentum, m, i.e., a magnetic quantum number, which takes half-integer values, $m = \pm 1/2, \pm 3/2, \pm 5/2, \ldots$. The corresponding eigenfunctions of Hamiltonian (2.1) can be written for the valley ξ in the following form

$$\psi^{(\xi)}(r,\theta) = e^{i(m-\xi/2)\theta} \begin{pmatrix} \chi_1^{(\xi)}(r) \\ e^{i\xi\theta}\chi_2^{(\xi)}(r) \end{pmatrix}, \tag{3.1}$$

where r and θ are polar coordinates.

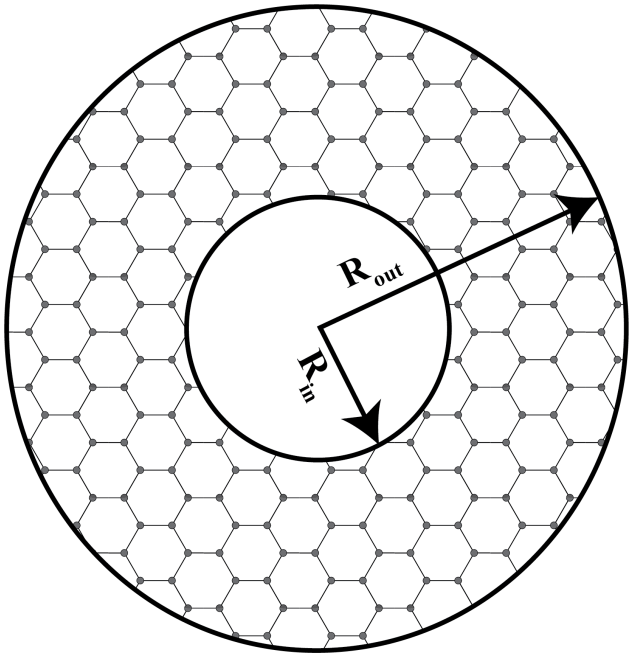

Figure 3.1 Schematic diagram of Graphene Quantum Ring.

3.2 Eigenvalue Equation

Substituting the form of the wavefunction (3.1) into the eigenvalue equation $H_0\psi^{(\xi)}(r,\theta) = E\psi^{(\xi)}(r,\theta)$, we obtain the following system of equations for functions $\chi_1^{(\xi)}(r)$ and $\chi_2^{(\xi)}(r)$

$$\nabla_r\chi_1^{(\xi)}(r) - \frac{(m-\xi/2)}{r}\chi_1^{(\xi)}(r) = \frac{iE}{\gamma}\chi_2^{(\xi)}(r), \tag{3.2}$$

$$\nabla_r\chi_2^{(\xi)}(r) + \frac{(m+\xi/2)}{r}\chi_2^{(\xi)}(r) = \frac{iE}{\gamma}\chi_1^{(\xi)}(r). \tag{3.3}$$

Then substituting $\chi_2^{(\xi)}$ from Eq. (3.2) into Eq. (3.3), we obtain the differential equation for $\chi_1(r)$

$$\nabla_r^2\chi_1^{(\xi)}(r) + \frac{1}{r}\nabla_r\chi_1^{(\xi)}(r) - \left(\frac{(m+\xi/2)^2}{r} - \frac{E^2}{\gamma^2}\right)\chi_1^{(\xi)}(r) = 0 \tag{3.4}$$

The above equation is the Bessel equation, and its solution can be expressed as a superposition of the Bessel and Neumann functions

$$\chi_1^{(\xi)}(r) = C_1^{(\xi)} J_{m-\xi/2}\left(\varepsilon \frac{r}{R_{\text{out}}}\right) + C_2^{(\xi)} N_{m-\xi/2}\left(\varepsilon \frac{r}{R_{\text{out}}}\right), \tag{3.5}$$

where $J_n(x)$ is the Bessel function of the first kind of order n, $N_n(x)$ is the Neumann function of order n, and $\varepsilon = \frac{R_{\text{out}}E}{\gamma}$. Here $C_1^{(\xi)}$ and $C_2^{(\xi)}$ are constants. From Eq. (3.2) we can also find the second component of the wavefunction,

$$\chi_2^{(\xi)}(r) = iC_1^{(\xi)} J_{m+\xi/2}\left(\varepsilon \frac{r}{R_{\text{out}}}\right) + iC_2^{(\xi)} N_{m+\xi/2}\left(\varepsilon \frac{r}{R_{\text{out}}}\right). \tag{3.6}$$

The energy spectrum of the nanoring is obtained from the infinite mass boundary conditions, which are introduced through the following expression[**?**]

$$\lim_{r\to\mathbf{R}} \chi_1^{(\xi)}(r) = i\xi \lim_{r\to\mathbf{R}} \chi_2^{(\xi)}(r), \tag{3.7}$$

where $\mathbf{R}$ is the boundary of the nanoring, i.e, $r = R_{\text{in}}$ and $r = R_{\text{out}}$. Substituting Eqs. (3.5)-(3.6) into Eq. (3.7), we obtain the equation for the eigenenergies of the system

$$\begin{aligned} &\frac{\xi N_{m+\xi/2}(\varepsilon R_{\text{in}}/R_{\text{out}}) + N_{m-\xi/2}(\varepsilon R_{\text{in}}/R_{\text{out}})}{\xi J_{m-\xi/2}(\varepsilon R_{\text{in}}/R_{\text{out}}) + J_{m+\xi/2}(\varepsilon R_{\text{in}}/R_{\text{out}})} \\ &= \frac{\xi N_{m+\xi/2}(\varepsilon) + N_{m-\xi/2}(\varepsilon)}{\xi J_{m-\xi/2}(\varepsilon) + J_{m+\xi/2}(\varepsilon)}. \end{aligned} \tag{3.8}$$

3.3 Results and Discussion

The energy spectrum of the graphene nanoring, obtained from Eq. (3.8), is shown in Fig. 3.2 for both K and K' valleys. It satisfies the condition of the time-reversal symmetry, i.e.,

$E_{K,m} = E_{K',-m}$. The energy spectrum also has the following specific structure. It has a finite bulk band gap, which is due to the finite size of the system. Here, the states with the positive energies belong to the conduction band, while the states with the negative energies belong to the valence band. As expected, the band gap decreases with increasing the system's size. For example for the outer radius $R_{\text{out}} = 15$ nm (see Fig. 3.2(a) and (b)) the band gap is around 2 eV, while for the outer radius $R_{\text{out}} = 35$ nm (see Fig. 3.2(c) and (d)) the band gap is 0.5 eV.

In addition to the gapped structure of the energy spectrum, there is a clear in-gap branch visible for each valley. These two branches are due to the edge states of the system [57, 58, 59]. The branches have different behaviors for the K and K' valleys. While for the K valley, the energy of the in-gap states decreases with the quantum number m, for the K' valley, the energy increases with m. Such fundamentally different behaviors of the energy spectrum at the two valleys result in different responses of the valley to a circularly polarized pulse. This is due to the fact, that, for example, for a clockwise circularly polarized pulse, the dipole selection rule is $m_{\text{final}} = m_{\text{initial}}+1$. Then, the rate of the optical transition between the states is determined by the corresponding energy difference, $\Delta E = E_{m_{\text{final}}} - E_{m_{\text{initial}}}$. The value of ΔE is different for the K and K' valleys, which finally results in different after-the-pulse CB populations for the two valleys. With the known wavefunctions, the dipole matrix elements between the states i and j can be calculated from the expression Eq. 2.7. Substituting Eq. (3.1) for the wavefunctions in terms of χ_1 and χ_2, we obtain the x and y components of the

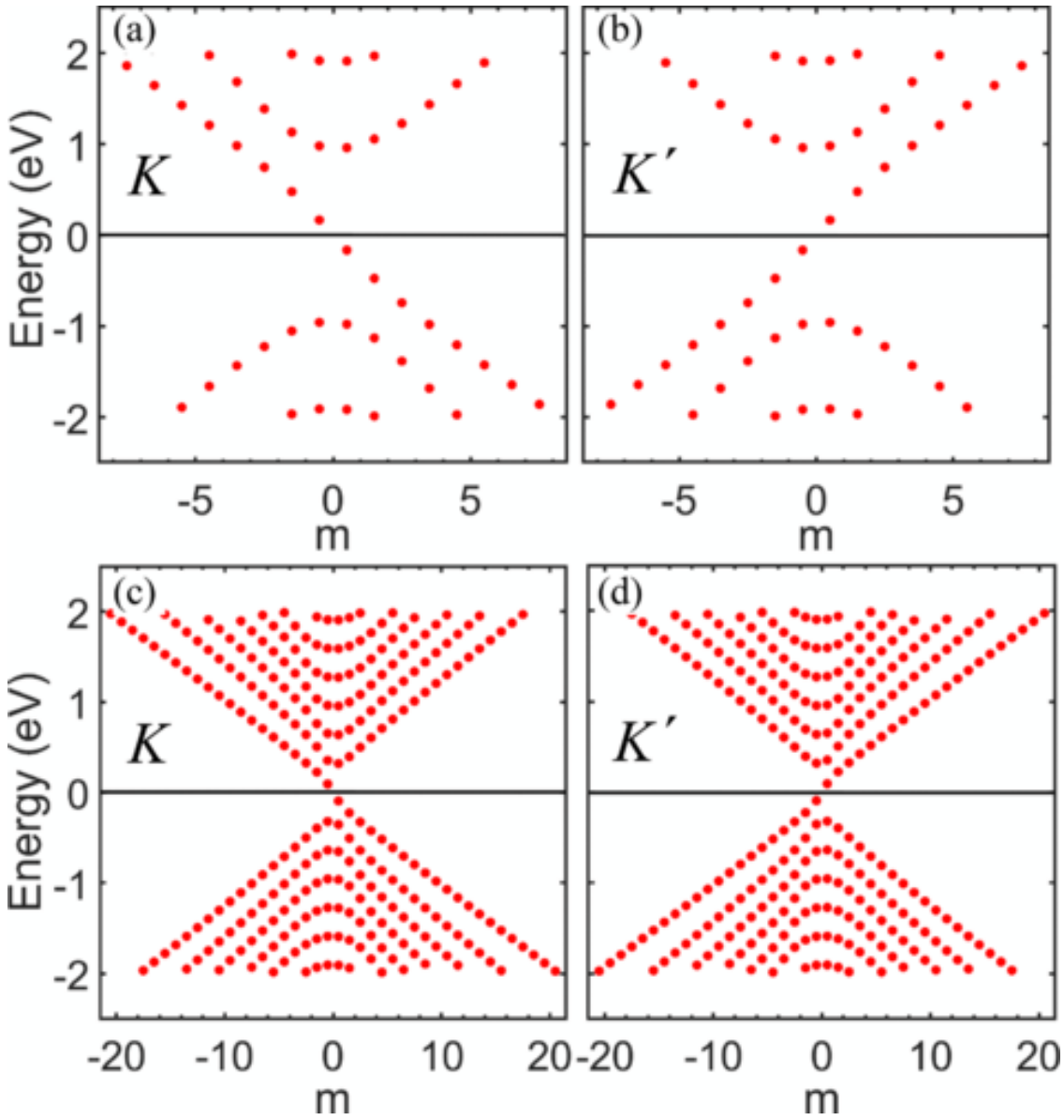

Figure 3.2 Energy spectra of graphene nanoring. The spectra are shown as a function of magnetic quantum number m, which takes half-integer values. The size of the nanoring is $R_{\text{in}} = 5$ nm, $R_{\text{out}} = 15$ nm in panels (a) and (b); $R_{\text{in}} = 5$ nm, $R_{\text{out}} = 35$ nm in panels (c) and (d). The spectra are shown for the K valley [panels (a) and (c)] and for the K' valley [panels (c) and (d)].

dipole matrix elements

$$D_{x,ij}^{(\xi)} = e\pi \left[\delta\left(m_i, m_j - 1\right) + \delta\left(m_i, m_j + 1\right)\right]$$
$$\int_{r_{in}}^{r_{out}} \left[\chi_{1,j}^{(\xi)*}(r)\chi_{1,i}^{(\xi)}(r) + \chi_{2,j}^{(\xi)*}(r)\chi_{2,i}^{(\xi)}(r)\right] r^2 dr \tag{3.9}$$

and

$$D_{y,ij}^{(\xi)}(r,\theta) = -ie\pi \left[\delta\left(m_i, m_j - 1\right) - \delta\left(m_i, m_j + 1\right)\right]$$
$$\int_{r_{in}}^{r_{out}} \left[\chi_{1,j}^{(\xi)*}(r)\chi_{1,i}^{(\xi)}(r) + \chi_{2,j}^{(\xi)*}(r)\chi_{2,i}^{(\xi)}(r)\right] r^2 dr. \tag{3.10}$$

Here m_i and m_j are magnetic quantum numbers of the corresponding states i and j. As expected, the dipole transitions have selection rule $m_i = m_j \pm 1$.

Now we place the graphene nanoring in the field of an optical pulse. The corresponding electron dynamics is described by the time-dependent Hamiltonian is given by Eq. 2.4. We consider only a circularly polarized optical pulse. Such a pulse breaks the inversion symmetry of the system, which can result in a finite final valley polarization of the system. The profile of the electric field of the circularly polarized pulse is given by the following expression

$$F_x(t) = F_0 e^{-u^2}\left(1 - 2u^2\right) \tag{3.11}$$

$$F_y(t) = F_0 e^{-u^2}(2u), \tag{3.12}$$

where $u = t/\tau$ and time parameter τ determines the pulse's duration and frequency. Below,

the main results are shown for $\tau = 1$ fs, i.e., the frequency of the pulse ≈ 1 eV. Here we consider only one oscillation of the field addressing the problem of ultrafast control of the valley degree of freedom. Thus, we consider the case when valley polarization can be generated by just a single oscillation of the optical pulse. Under this condition, only one parameter, τ, characterizes the pulse's duration and frequency. As mentioned above, the continuous model of graphene generates an infinite number of states within the nanoring. In Fig. 3.2, we show only the energy levels taken into account in our calculations. These levels are within the energy window, -2 eV$< E <$ 2 eV. Such energy interval is chosen in such a way that for the optical pulse with the amplitude up to $F_0 = 0.3$ eV, the valley polarization converges to the values presented below with the accuracy less than 5%.

We apply a single cycle of a left circularly polarized optical pulse. The pulse profile, i.e., the x and y components of the pulse electric field, is shown in Fig. 4.3. Before the pulse, all states of graphene nanoring with negative energies are populated. The optical pulse results in the redistribution of electrons between the states of the nanoring and in the population of the CB states, both the in-gap states and the bulk states.

We assume that the pulse duration, around 6 fs, is less than the characteristic relaxation times of the nanoring. In this case, the electron dynamics within the graphene nanoring is described by the time-dependent Schrödinger equation,

$$i\hbar\frac{d\Psi^{(\xi)}(t)}{dt} = \mathcal{H}^{(\xi)}(t)\Psi^{(\xi)}(t). \tag{3.13}$$

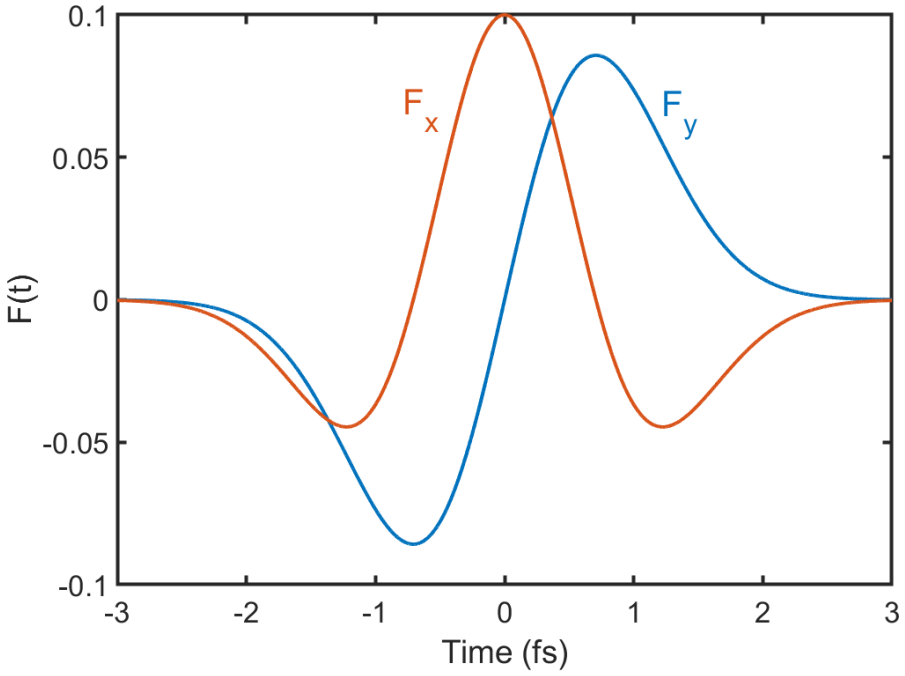

Figure 3.3 Profile of the electric field of a left circularly polarized optical pulse. The pulse has only one oscillation. The amplitude of the pulse is $F_0 = 0.1$ V/Å. The optical field has both x and y components. The inset shows the corresponding one cycle of the optical pulse.

We expand a solution of Eq. (2.2) in the basis of single-particle states (3.1), ψ_i,

$$\Psi^{(\xi)}(t) = \sum_{j=1}^{N} \beta_j^{(\xi)}(t)\psi_i^{(\xi)} e^{-\frac{i}{\hbar}E_j t}, \tag{3.14}$$

with the time-dependent expansion coefficients $\beta_i^{(\xi)}(t)$.

One of the main characteristics of electron dynamics in the field of the pulse is the total CB population, $\mathcal{N}_{CB}^{(\xi)}$. In Fig. 3.4, the CB population is shown as a function of time for the two valleys, K and K', and different amplitudes of the pulse, F_0. The size of the nanoring is $R_{\text{in}} = 5$ nm and $R_{\text{out}} = 15$ nm. For all values of F_0 the electron dynamics is highly irreversible, i.e., the maximum CB population is almost the same as the final CB population,

i.e., the population after the pulse. The irreversible dynamics have also been observed in graphene monolayer [9]. Another essential property of CB population dynamics is that the final CB population for the K valley is always greater than the corresponding population for the K' valley. It means that, after the pulse, there is a finite valley polarization of the graphene nanoring.

As expected, the CB population monotonically increases with the field amplitude, see Fig. 3.4. Here, the results are shown for the frequency of the pulse around 1.0 eV, which corresponds to the time parameter of $\tau = 1$ fs, see Eqs. (3.11)-(3.12). To illustrate the effect of the pulse frequency on the electron dynamics, we show in Fig. 3.5 the CB population for different values of τ. In all cases, the pulse has only one oscillation. With increasing τ, the pulse frequency decreases, which enhances the coupling of the VB states and the in-gap CB states, where the energy separation between them is relatively small, i.e., less than 1 eV. As a result, the populations of the in-gap edge states increase with τ. Such a tendency is visible in Fig. 3.5 for both valleys, while it is more pronounced for the K valley. To characterize the final state of the electron system, we show in Fig. 3.6 the occupations of individual CB levels after the pulse. The results are shown for different field amplitudes. As discussed above, with increasing the field amplitude, F_0, the occupations of the CB levels monotonically increase, which occurs for each level. At the same time, the largest occupations are visible for the in-gap edge CB states, which are marked by red lines. Also, the main difference between the K and K' valleys is mainly in the populations of the in-gap edge states.

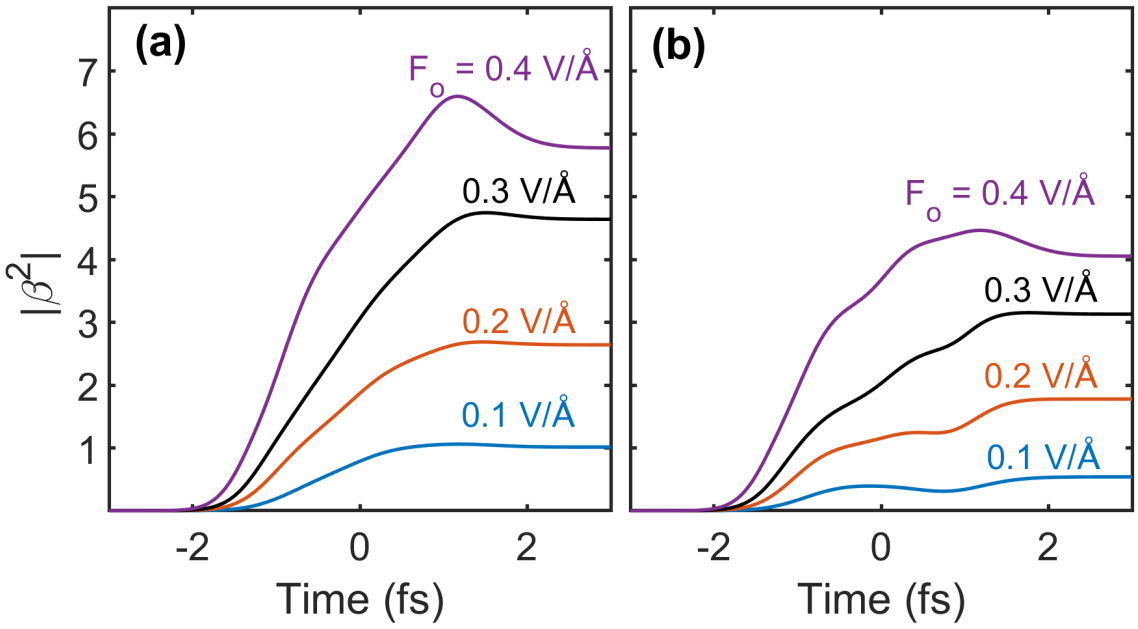

Figure 3.4 Conduction band population as a function of time. The conduction band states are the states with positive energies. The data are shown for different field amplitudes for the K valley [panel (a)] and the K' valley [panel (b)]. The corresponding values of F_0 are shown next to each line. The inner and outer radii of the nanoring are $R_{\text{in}} = 5$ nm, $R_{\text{out}} = 15$ nm. The time constant, which determines the frequency and the duration of the optical pulse, is $\tau = 1$ fs. The optical pulse is left circularly polarized.

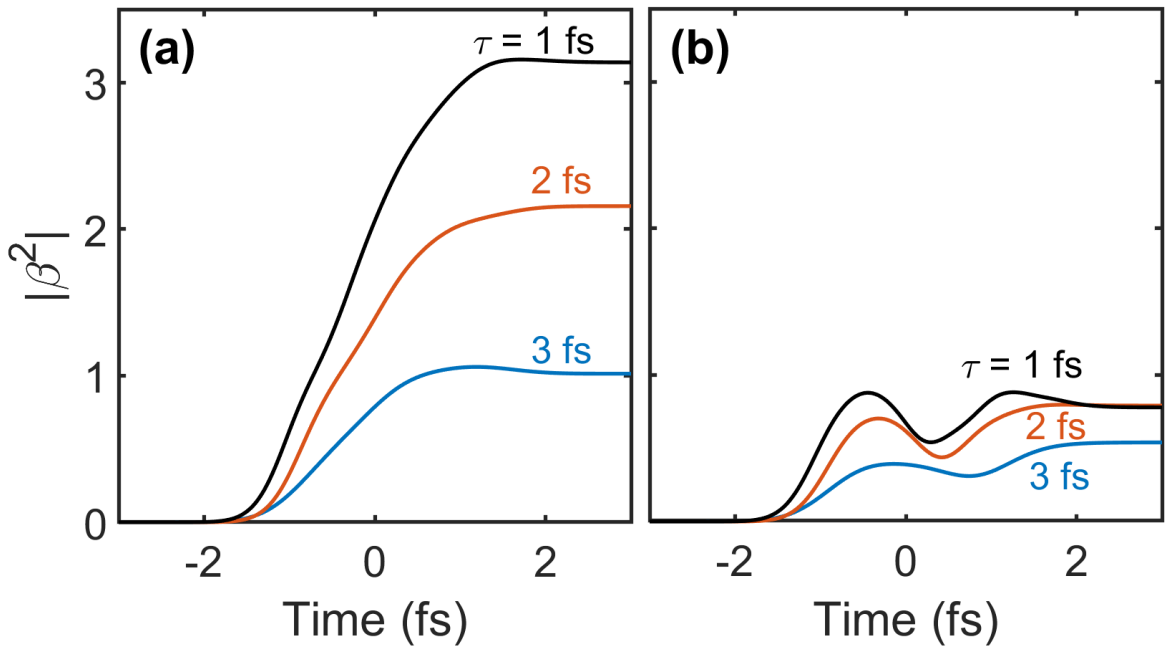

Figure 3.5 Conduction band population as a function of time. The conduction band states are the states with positive energy. The data are shown for different value of parameter τ for the K valley [panel (a)] and the K' valley [panel (b)]. The corresponding values of τ are shown next to each line. Parameter τ determines both the frequency of the pulse and its duration. The time is shown in dimensionless units, t/τ. The inner and the outer radii of the nanoring are $R_{\text{in}} = 5$ nm and $R_{\text{out}} = 15$ nm. The field amplitude is $F_0 = 0.1$ V/Å. The optical pulse is left circularly polarized.

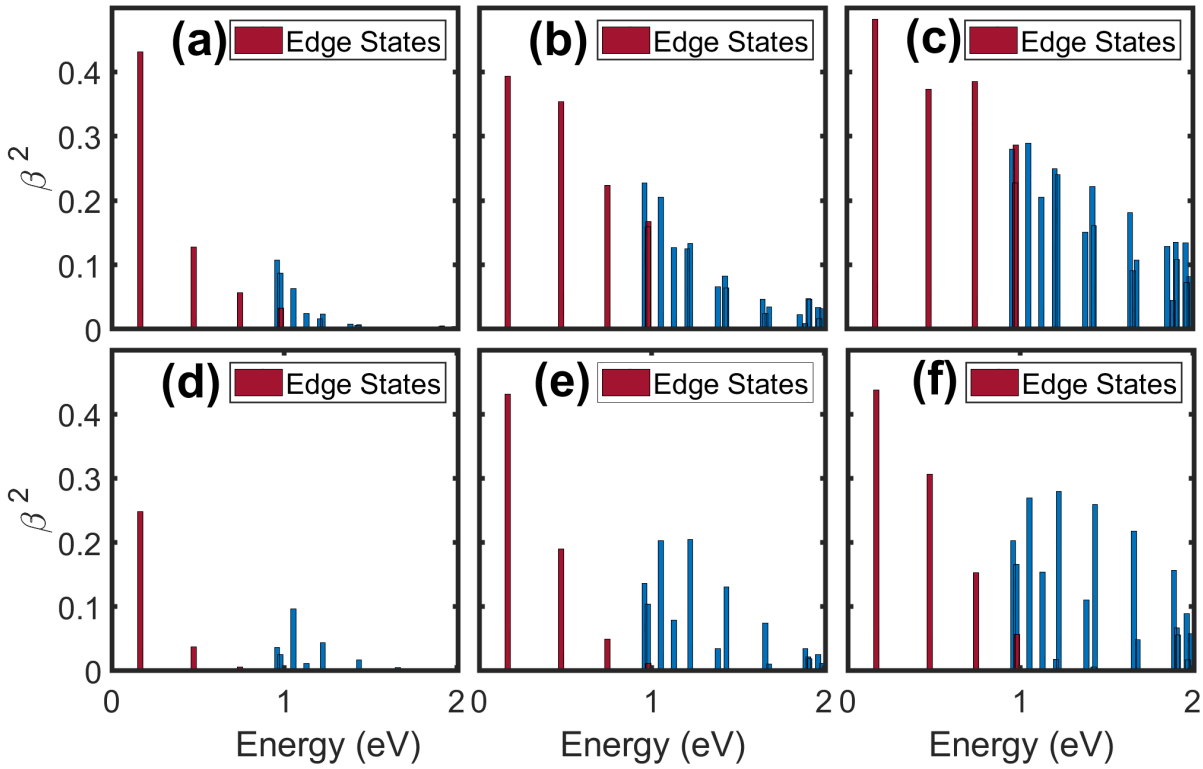

Figure 3.6 Population of individual conduction band levels. The results are for the K valley [panels (a), (b), and (c)] and the K' valley [panels (d), (e), and (f)]. The amplitude of the pulse is $F_0 = 0.1$ V/Å[panels (a) and (d)], $F_0 = 0.2$ V/Å[panels (b) and (e)], $F_0 = 0.3$ V/Å[panels (c) and (f)]. The inner and the outer radii of the nanoring are $R_{\text{in}} = 5$ nm and $R_{\text{out}} = 15$ nm. The red lines correspond to in-gap edge states, while the blue lines correspond to bulk states of the nanoring. The time constant of the pulse is $\tau = 1$ fs. The optical pulse is left circularly polarized.

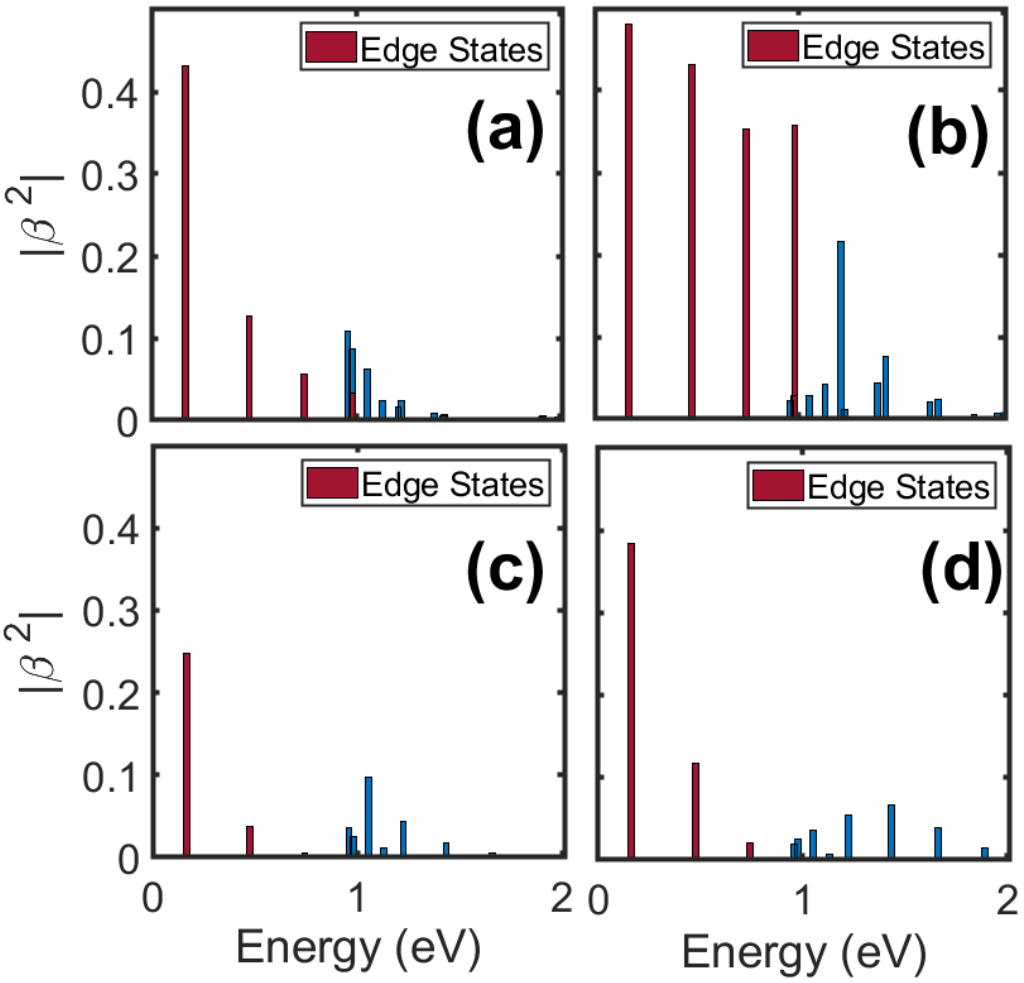

Figure 3.7 Population of individual conduction band levels. The results are for the K valley [panels (a) and (b)] and the K' valley [panels (c) and (d)]. The time constant of the optical pulse is $\tau = 1$ fs [panels (a) and (c)] and $\tau = 2$ fs [panels (b) and (d)]. The inner and the outer radii of the nanoring are $R_{\text{in}} = 5$ nm and $R_{\text{out}} = 15$ nm. The red lines correspond to in-gap edge states, while the blue lines correspond to bulk states of the nanoring. The amplitude of the pulse is $F_0 = 0.1$ V/Å. The optical pulse is left circularly polarized.

For example, comparing panels (c) and (f), we can say that the populations of the bulk CB states, which are shown by blue lines, are almost the same for the K and K' valleys, while the populations of the edge CB states (red lines) are quite different. Such a difference

results in the final valley polarization of the system.

To emphasize the effect of the frequency of the pulse on the ultrafast electron dynamics, we show in Fig. 3.7 the final populations of the CB levels for different values of τ. When the time parameter τ increases from 1 fs to 2 fs, the populations of the in-gap edge states are strongly increased. This is because the pulse frequency becomes smaller, and the low-energy CB states become more populated. Such an enhancement is more pronounced for the K valley, see Fig. 3.7. For example, the populations of all edge CB states (the red lines in Fig. 3.7) strongly increase when τ changes from 1 fs to 2 fs for the K valley and almost all of them become around 0.4, while, for the K' valley, even for $\tau = 2$ fs only two red lines are visible in the figure with the populations of 0.4 and 0.1.

The main outcome of the interaction of the circularly polarized pulse with the graphene nanoring is the valley polarization of the electron system. We have used two expressions to define the valley polarization, P and P_N, see Eqs. (2.9)-(2.10). Here, P is just the difference between the CB populations of the K and K' valleys per unit area, while P_N is its normalized value.

In Fig. 3.8, the valley polarization P is shown as a function of the field amplitude for different parameters of the nanoring. At small field amplitudes, the valley polarization quadratically increases with F_0. At large values of F_0, the valley polarization shows a saturated behavior. Such saturation is related to the finite number of nanoring levels considered in the model. Although our results are the most accurate for the field amplitude less than 0.3 V/Å, we show the data for the field amplitude of up to 0.5 V/Å to illustrate the effect

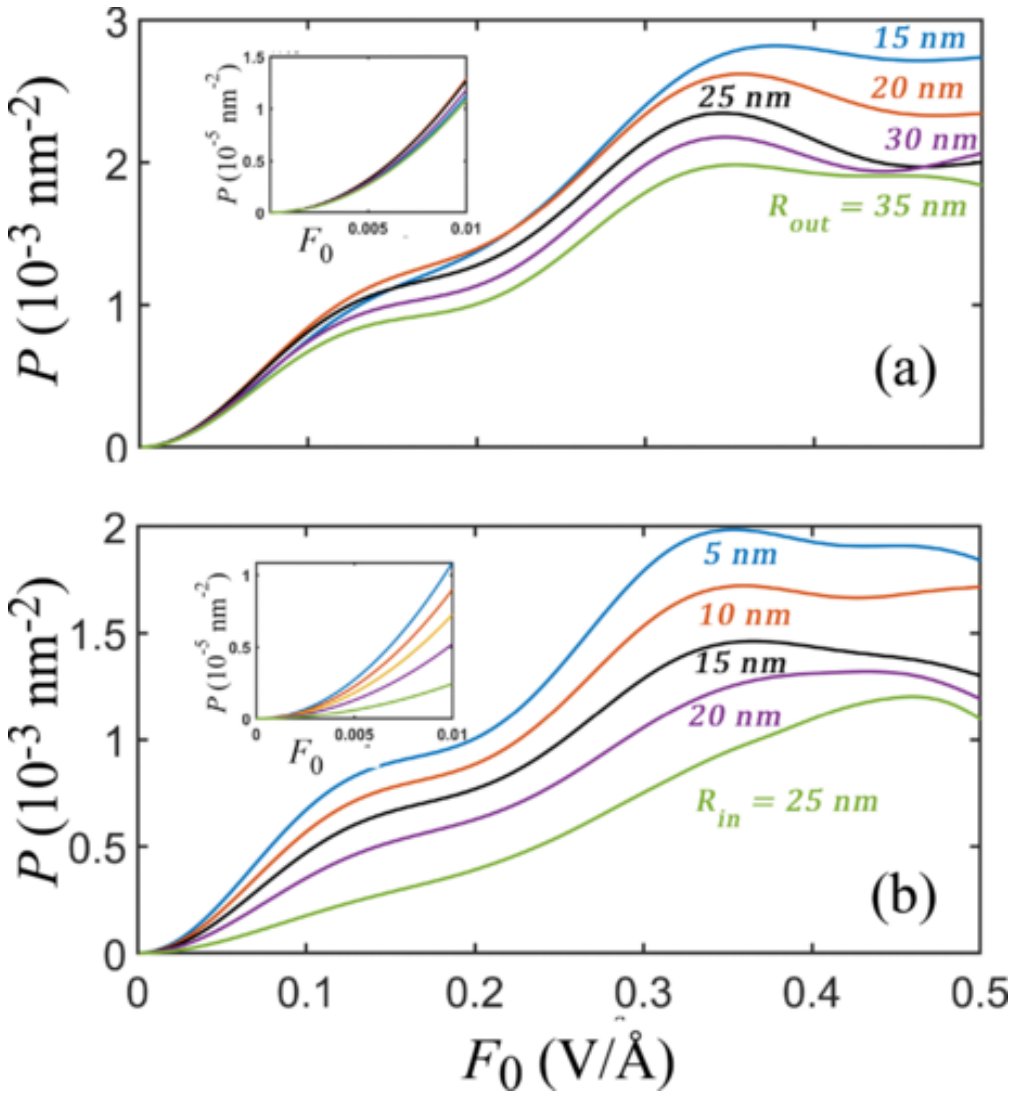

Figure 3.8 The valley polarization of a graphene nanoring. The valley polarization is defined by Eq. (2.9) and is shown as a function of the field amplitude F_0 for different parameters of the nanoring. In panel (a), the inner radius is fixed at $R_{\mathrm{in}} = 5$ nm and the outer radius is varied with the corresponding values shown next to each line. In panel (b), the outer radius is fixed at $R_{\mathrm{out}} = 35$ nm, and the inner radius is varied with the corresponding values shown next to each line. The time constant of the pulse is $\tau = 1$ fs, and the pulse is left circularly polarized. The insets in each panel show the valley polarization at small values of F_0.

of a finite number of levels within a nanoscale system.

In Fig. 3.8(a), the inner radius of the nanoring is fixed, and the outer radius is varied. The results show that with increasing the outer radius, the valley polarization P, defined as the polarization per unit area, decreases. This is consistent with the fact that the valley polarization of the graphene monolayer, i.e., an infinite graphene nanoring, is zero.

Figure 3.8(b) illustrates the valley polarization's dependence on the nanoring's inner radius. In this case, with decreasing the inner radius, while the size of the nanoring increases, the valley polarization still increases. Thus, these results suggest that the maximum valley polarization is achieved for a nanoring with the smallest inner radius, i.e., for a disk. To check this statement, we calculated the valley polarization for a disk using the infinite mass boundary conditions at the disk's boundary. The results show that for the graphene disk with the radius of 15 nm, the valley polarization is $P = 0.0028$ nm^{-2} for the field amplitude of 0.2 V/Å, while for the ring with the inner radius of 5 nm and the outer radius of 15 nm, the corresponding valley polarization has a smaller value of $P = 0.0014$ nm^{-2}. These data support the above statement that the valley polarization is the largest for the disk. A detailed analysis of the valley polarization generated in graphene nanodisks by the optical pulse will be given elsewhere.

At small field amplitudes, F_0, the valley polarization has a quadratic dependence on F_0, i.e., a linear dependence on the power of the pulse, with the coefficient that depends on the parameters of the nanoring. We can approximate such dependence with the following

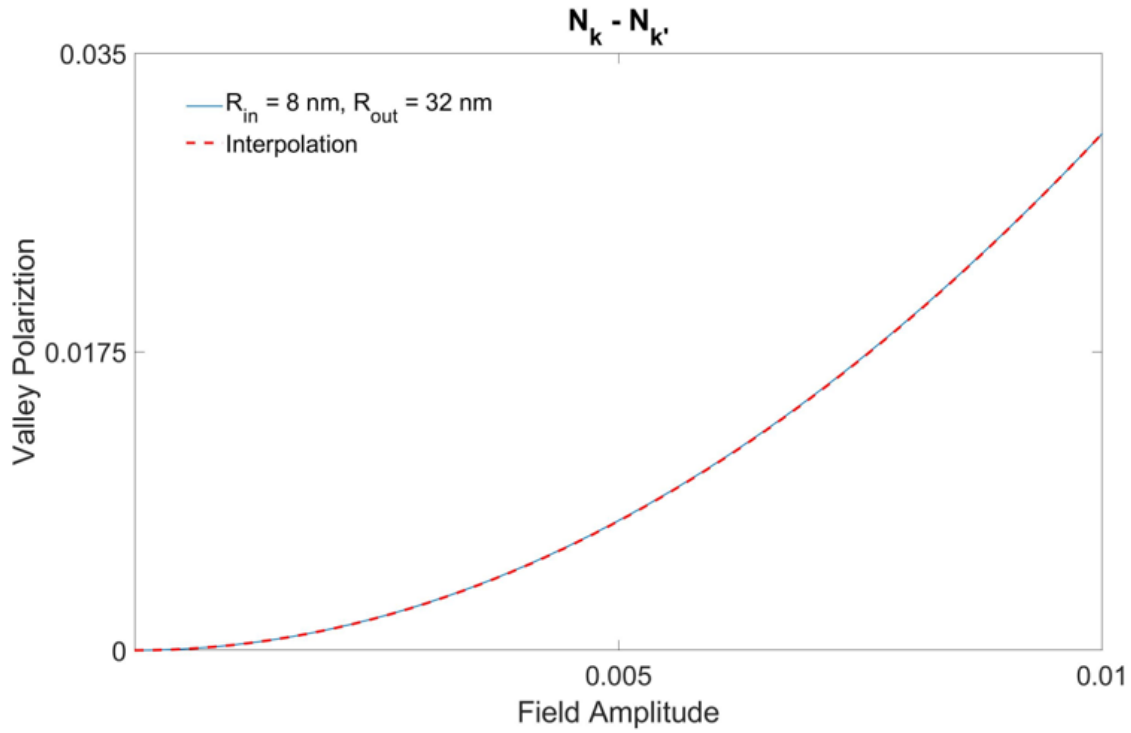

Figure 3.9 The valley polarization of a graphene nanoring. The valley polarization is defined by Eq. (2.10) and is shown as a function of the field amplitude F_0 for different parameters of the nanoring. In panel (a), the outer radius is fixed at $R_{\text{out}} = 35$ nm, and the inner radius is varied with the corresponding values shown next to each line. In panel (b), the inner radius is fixed at $R_{\text{in}} = 5$ nm, and the outer radius is varied with the corresponding values shown next to each line. The time constant of the pulse is $\tau = 1$ fs, and the pulse is left circularly polarized.

expression

$$P = \frac{5.42R_{\text{out}} - 5.89R_{\text{in}} + 30}{R_{\text{out}}^2 - R_{\text{in}}^2} F_0^2, \tag{3.15}$$

where F_0 is measured in V/Å and R_{out}, R_{in} are in nm. Equation (3.15) can be used to design the nanoring with a given value of the valley polarization. A comparison of interpolated plot with the actual calculation by using Dirac Effective model is illustrated in Fig. 3.9.

The valley polarization can also be characterized by its normalized value, see Eq. (2.10),

which shows the fraction of the excited electrons that are valley polarized. The normalized valley polarization as a function of the field amplitude, F_0, is shown in Fig. 3.10 for different sizes of the nanoring. Similar to the case of valley polarization P, see Fig. 3.8, for a fixed internal radius of the nanoring, R_{in}, the valley polarization P_N decreases with increasing the size of the system, i.e., R_{out}, see Fig. 3.10(b). This is consistent with the expectation that with increasing the size of the nanoring, the system becomes more similar to a pristine graphene monolayer, for which there is no valley polarization after a circularly polarized pulse.

Also, when the outer radius is fixed, and the inner radius is varied, see Fig. 3.10(a), the valley polarization increases with decreasing the inner radius of the nanoring, R_{in}. This behavior is similar to what was shown in Fig. 3.8(b) and also means that the maximum valley polarization is observed for the small inner radius. The normalized valley polarization can reach the value of up to 40 %, see Fig. 3.10(b).

The main difference between the valley polarizations P and P_N is that, at small field amplitudes, the normalized valley polarization almost does not depend on the field amplitude. Its dependence on the parameters of the nanoring can be approximated by the following expression

$$P_N = -0.005886 R_{\text{out}} - 0.0072 R_{\text{in}} + 0.4964. \tag{3.16}$$

Such an expression can be used to predict the valley polarization for the nanoring of a given size.

Comparing behaviors of P and P_N, we can see that, at a finite field amplitude F_0, P

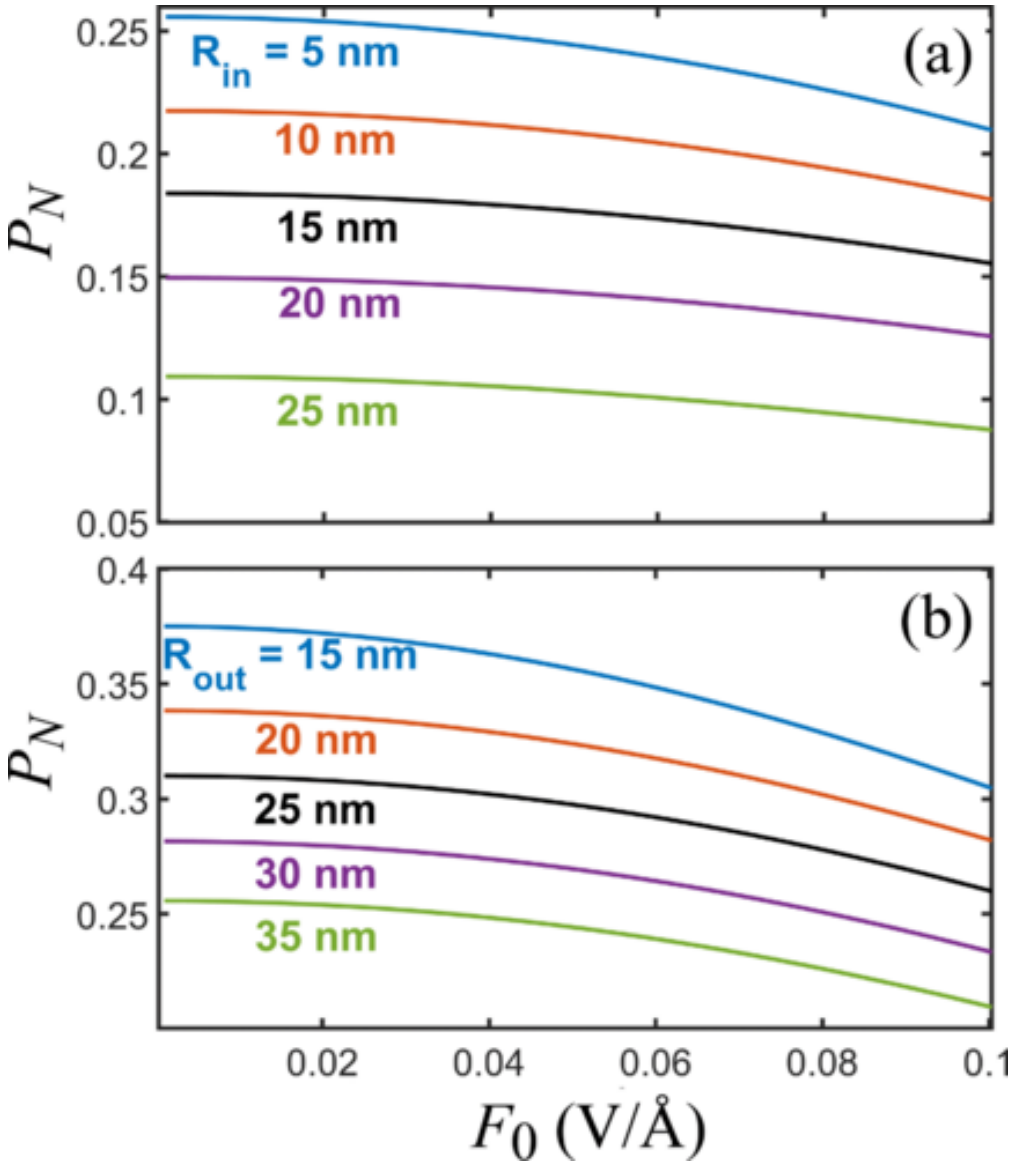

Figure 3.10 The valley polarization of a graphene nanoring. The valley polarization is defined by Eq. (2.10) and is shown as a function of the field amplitude F_0 for different parameters of the nanoring. In panel (a), the outer radius is fixed at $R_{\text{out}} = 35$ nm, and the inner radius is varied with the corresponding values shown next to each line. In panel (b), the inner radius is fixed at $R_{\text{in}} = 5$ nm, and the outer radius is varied with the corresponding values shown next to each line. The time constant of the pulse is $\tau = 1$ fs, and the pulse is left circularly polarized.

increases with F_0, while P_N decreases. For the valley polarization P, its increase with F_0 is because at larger field amplitudes, more nanoring levels are excited, resulting in larger populations of both the K and K' valleys and correspondingly in larger valley polarization P. For the valley polarization P_N, which is defined as a fraction of excited electrons that are valley polarized, both the number of the excited electrons and the difference between the CB populations of the two valleys increase with F_0. The main contribution to the difference in the CB populations of the valleys comes from the edge states, while the total population of the CB is determined by both the edge states and the bulk states of the nanoring. As a result, the valley polarization P_N decreases with increasing the field amplitude.

Expressions (3.15) and (3.16) have been obtained for a particular profile of the optical pulse, which is a single oscillation circularly polarized optical pulse with the time constant of $\tau = 1$ fs. Similar expressions can be obtained for optical pulses of different polarizations, frequencies, and durations. The parameters of the edge states of the graphene nanoring depend on the shape of the ring, and the model used to describe it [58]. Thus, they will also affect the valley polarization and the corresponding expressions (3.15) and (3.16).

3.4 Conclusion

In graphene-like systems with two valleys, the valley polarization can be induced only through the processes which break the time-reversal symmetry. For example, such polarization can be introduced in systems interacting with a circularly polarized pulse. Here, ultrashort optical pulses are particularly interesting since they allow control of the valley degree of

freedom at a femtosecond time scale. The valley polarization can be induced by such an ultrashort circularly polarized pulse in monolayers of graphene-like materials only if they have broken inversion symmetry. The broken inversion symmetry also introduces a finite band gap in the system. Thus, in pristine graphene, which has inversion symmetry, no valley polarization can be generated by any short optical pulse. To resolve such a problem, we consider a graphene monolayer with broken translational symmetry, i.e., graphene nanoring. The energy spectrum of such a nanoring consists of bulk states with a finite band gap between the valence and the conduction bands and in-gap edge states. Such in-gap states are mainly responsible for generating a finite valley polarization of the nanoring. The valley polarization induced by the ultrashort optical pulse depends on the parameters of the nanoring, i.e., its inner and outer radii. With increasing the size of the nanoring, the normalized valley polarization decreases and converges to a zero value for the infinite graphene monolayer.

Although we considered a particular shape of the graphene nanosystem, i.e., nanoring, we expect that the valley polarization can be induced by an ultrashort circularly polarized pulse for a graphene nanoflake of any shape. In our analysis, we also did not consider an inter-valley mixing induced by the boundaries of the graphene nanosystem. Such mixing can be significant only for relatively small graphene nanorings.

CHAPTER 4

High Harmonic Generation by Linearly Polarized Laser Pulse

4.1 Introduction

Pristine graphene has constrained optoelectronic applications due to its lack of optical emission, GQDs offer a compelling contrast. GQDs are renowned for their broadband absorption capabilities and can serve as fluorescent materials across a wide spectral range, spanning from ultraviolet to infrared regions [60, 61, 62, 63]. This opens up diverse possibilities for their use in advanced optoelectronic applications. Quantum confinement in graphene nanostructures breaks the inherent inversion symmetry, leading to the emergence of a non-zero bandgap and a quantized energy spectrum, which can be adjusted by changing the size of the system [64]. When these structures encounter an intense optical pulse, a remarkable non-linear optical phenomenon known as High Harmonic Generation (HHG) occurs [65, 66, 67, 68, 69, 70, 71, 72, 73, 74, 75, 76]. HHG materializes through the interaction of an intense laser field with the nanostructure, triggering the emission of radiation at integer multiples of the incident laser frequency [70]. HHG in graphene QDs is especially appealing, since it can be controlled by the size and the shape of a QD.

In the context of solid state physics, a strong short optical pulse modifies both the transport and optical properties of solids [77, 78, 79, 80, 65, 81, 82, 83, 84, 85, 20, 86, 87, 88]. In terms of electron dynamics, an ultrashort optical pulse induces two distinct dynamics known as interband and intraband electron dynamics which unfolds the process of HHG through the interactive interactions of these two distinct dynamics [69, 70, 71, 75, 76, 89]. The

intraband dynamics provokes the redistribution of electrons from the conduction band to the valance band while the intraband dynamics facilitates the electron transitions through non-parabolic bands, leading to a non-linear optical response. Both dynamics are instrumental in producing high harmonics, but their respective contributions depend on the solid's bandgap and the pulse parameters, such as its frequency and amplitude.

While numerous studies have extensively employed the TB model and DFT for exploring GQDs, usually these models are applied for the QDs of relatively small sizes, less than 5 nm. The TB model of small GQDs has been applied to study HHG in such systems, where the effect of dephasing on generation of high harmonics has been analyzed[90]. To study the HHG in large QDs with a size of upto 30 nm, the effective low-energy models should be applied. Such effective model can describe only the low-energy electron dynamics in such QDs, which introduces limitations on the intensity of external optical pulses. Also, the effective model cannot be applied to small QDs when the inter-valley mixing becomes important.

In this chapter, we study the generation of high harmonics in GQDs, which have the shape of a disk, as shown in Fig. 4.1. The QDs are described within an effective model, which allows us to consider QDs of large sizes. The unique features in high harmonic spectra that are specific to GQDs should be expected when the frequency of the pulse or the energy scale introduced by the field of the pulse is comparable to the QD band gap, which occurs due to the dimensional quantization of the system.

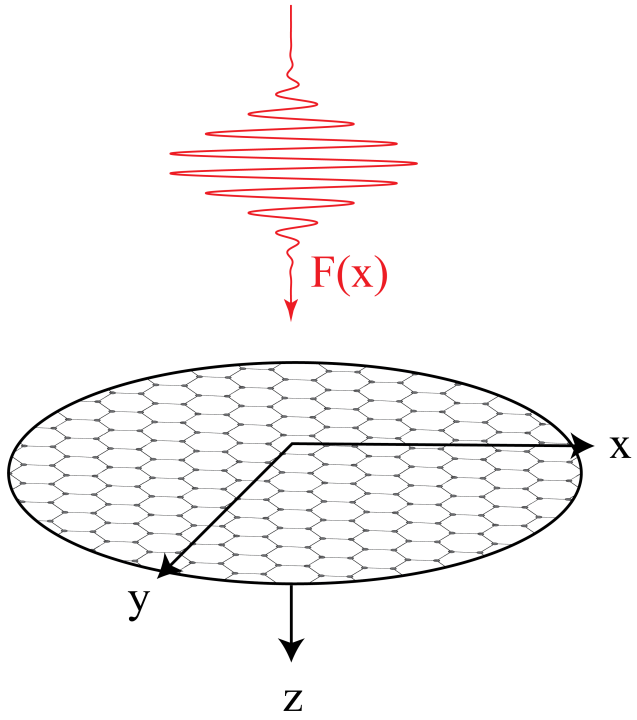

Figure 4.1 Schematic Representation of a Graphene Quantum Disk Interacting with an x-Polarized Laser Pulse

4.2 Energy Spectrum

The confinement potential $V(r)$ in (2.1) corresponds to the infinite mass constrain and is given by the following expression

$$V(r) = \begin{cases} 0 & r = R \\ \infty & \text{else where} \end{cases}, \tag{4.1}$$

where R is the radius of a QD. The eigenfunctions and the energy spectrum are obtained from the corresponding Schrodinger equation

$$\mathcal{H}^{(\xi)}\psi^{(\xi)} = E^{(\xi)}\psi^{(\xi)}, \tag{4.2}$$

where $E^{(\xi)}$ is the eigenenergy and $\psi^{(\xi)}$ is the corresponding eigenfunction.

Solutions of the differential equations (3.2) and (3.3) has the following form

$$\begin{pmatrix} \chi_1^{(\xi)}(r) \\ \chi_2^{(\xi)}(r) \end{pmatrix} = A \begin{pmatrix} J_{m-\xi/2}(\varepsilon^{(\xi)} r/R) \\ iJ_{m+\xi/2}(\varepsilon^{(\xi)} r/R) \end{pmatrix}, \tag{4.3}$$

where $J_n(x)$ is the Bessel function of the n^{th} order, A is the normalization constant and $\varepsilon^{(\xi)} = E^{(\xi)}R/\gamma$ is the dimensionless energy. The energy spectrum is obtained from the infinite mass boundary conditions, which can be expressed as Eq. 3.7 [45, 46, 47] Substituting $\chi_1^{(\xi)}(r)$ and $\chi_2^{(\xi)}(r)$ from Eq. (4.3) we obtain the following eigenvalue equation

$$J_{m-\frac{\xi}{2}}(\varepsilon) + \xi J_{m+\frac{\xi}{2}}(\varepsilon) = 0. \tag{4.4}$$

The eigenvalue equation (4.4) is solved numerically for the K and K' valleys. The typical energy spectra of graphene QDs are shown in Fig. 4.2. The energy levels are characterized by magnetic quantum number m. The levels with the negative and positive energies belong to the valence and the conduction bands, respectively. Due to the finite size of the system, the energy spectra have finite band gaps, which decrease with increasing the QD size. For example, for a QD with the radius of 15 nm the band gap is 0.578 eV, but when the radius becomes 30 nm, the band gap is 0.29 eV. The energy spectra of graphene QDs also show the time reversal symmetry of the system. Namely, the energy spectra satisfy the following condition $E_{K,m} = E_{K',-m}$, where $E_{K,m}$ and $E_{K',m}$ are the energy spectra of the K and K' valleys. Another important feature of the energy spectra of graphene QDs is that the minimum of the conduction band and the maximum of the valence band are at different values of m.

This property results, for example, in the generation of finite valley polarization after

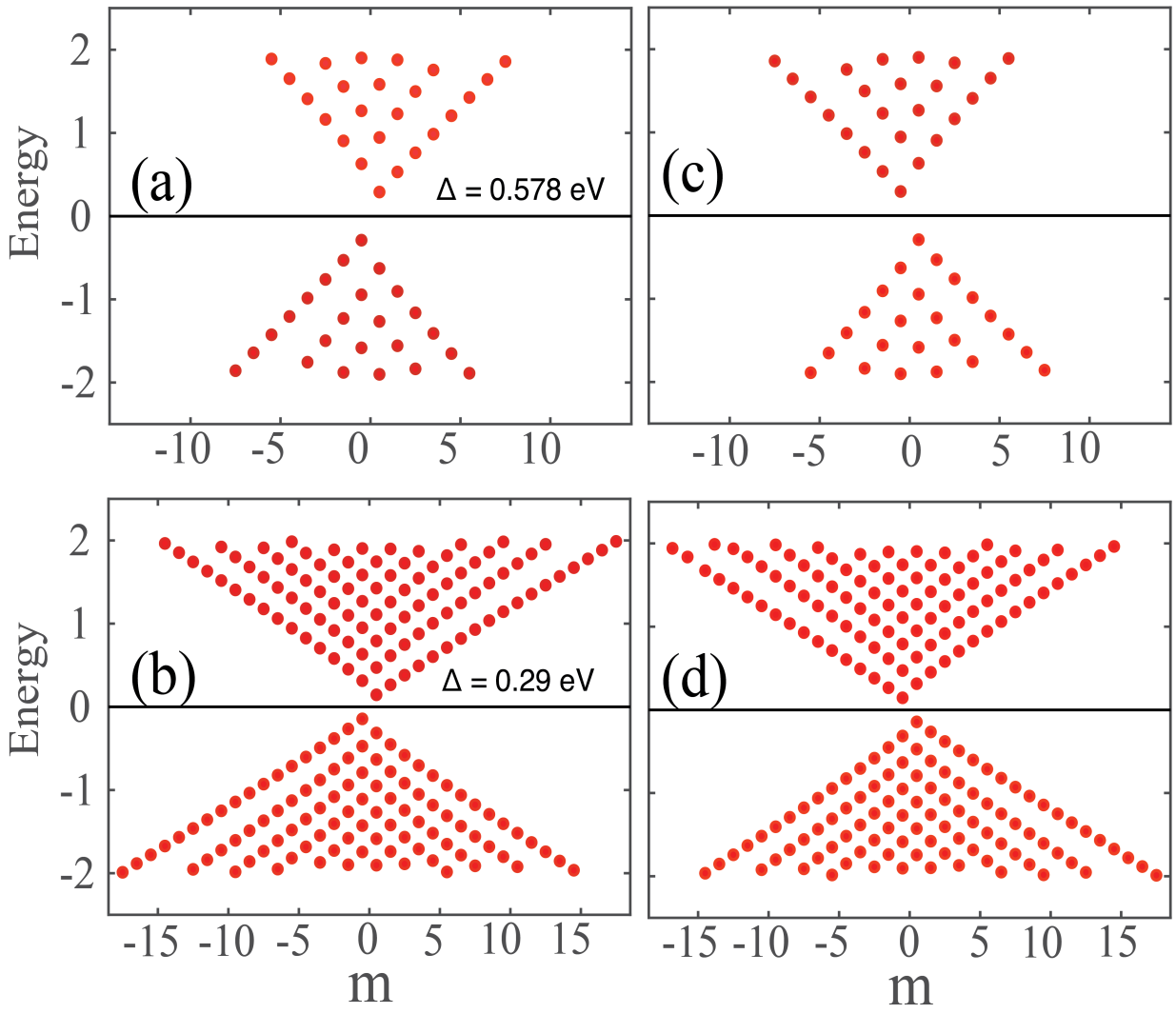

Figure 4.2 Energy spectra of graphene quantum dots. The energy spectra are shown for the K (a), (d) and K' (c), (d) valleys. The radius of the quantum dot is 15 nm (a), (c) and 30 nm (b), (d).

a circularly polarized ultrashort optical pulse is applied to the system [64]. For a linearly polarized pulse, the responses of K and K' to the pulse are the same, i.e., the generated dipole moments and the corresponding radiation spectra are the same.

4.3 Results and Discussion

We study the nonlinear response of the QD system to an external ultrashort optical pulse. The optical pulse is linearly polarized in the x direction with field profile of the following form

$$F_x(t) = F_0 e^{-(t/\tau)^2} \cos(\omega_0 t), \tag{4.5}$$

where τ determines the duration of the pulse, ω_0 is the frequency of the pulse, and F_0 is the amplitude of the pulse. The dynamics of a QD placed in the field of an optical pulse is described by the Hamiltonian, which consists of the field-free Hamiltonian (2.1) and the part that describes the interaction of the electron system with the field of the pulse. The profile of the electric field of a linearly polarized pulse is shown in Fig. 4.3. Such a pulse generates time-dependent dipole moment, which finally results in far-field radiation. Without relaxation, the generated residual dipole moment, i.e., the dipole moment after the pulse, has an oscillating behavior, which strongly affects the radiation spectra. Such oscillations are suppressed due to relaxation and dephasing processes. In our coherent approach, to eliminate the contribution to the radiation spectra from the oscillating part of the residual dipole moment, we included the relaxation time phenomenologically as an extra factor e^{-t/τ_r} in the expression for the dipole moment. For all data presented below the relaxation time

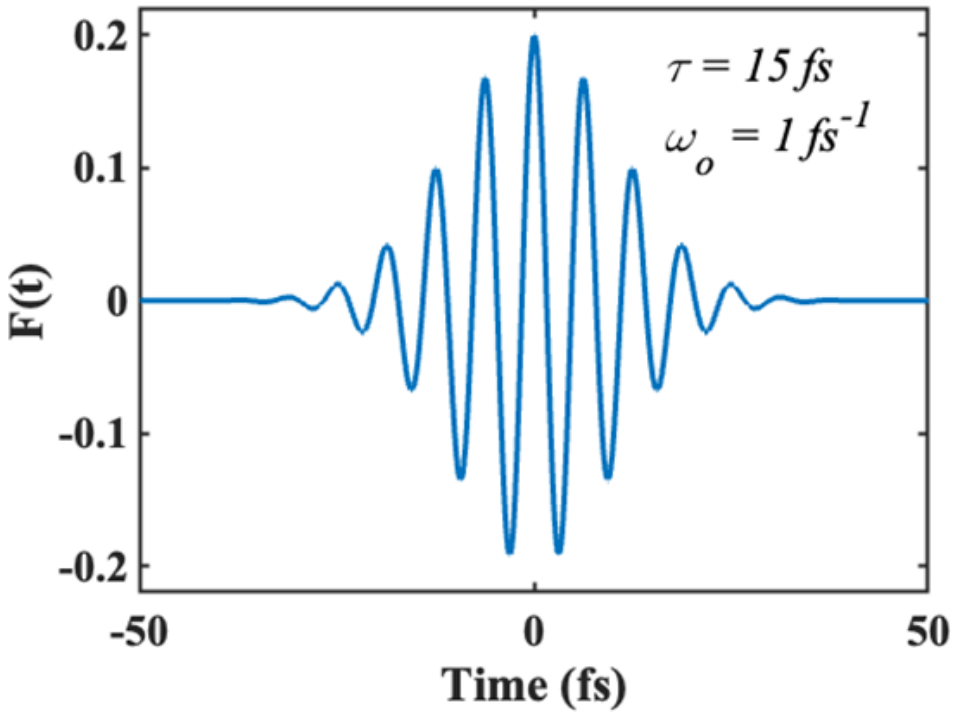

Figure 4.3 Profile of the electric field of the pulse as a function of time. The amplitude of the pulse is 0.2 V/Å. The frequency of the pulse is 1 rad/fs and the pulse duration is determined by parameter $\tau = 15fs$.

τ_r was 15 fs.

The generated radiation spectra for different parameters of the system and the optical pulse are shown in Fig. 4.4. The general tendency that is visible in Fig. 4.4 is that the cutoff frequency increases with increasing the size of the system, which is expected since with increasing the QD radius there are more levels that contribute to the generation of high harmonics. The range of the frequencies shown in Fig. 4.4 covers different situations when the frequency of the pulse is less or greater then the band gap of the system. For the frequency of the pulse of 0.25 rad/fs, which corresponds to the energy of 0.16 eV, for all

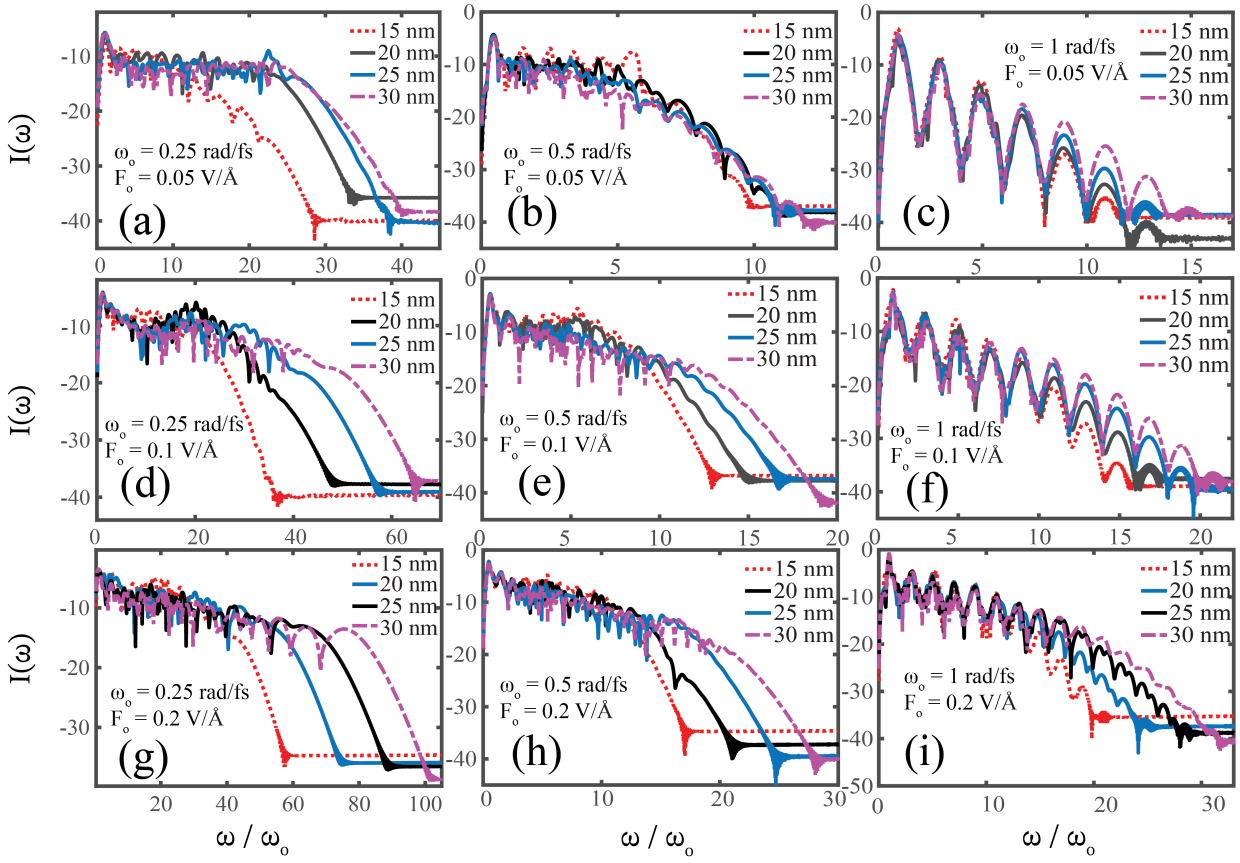

Figure 4.4 Radiation spectra of graphene quantum dots. The frequency and the amplitude of the pulse are marked in each panel. Different lines in each panel correspond to different radii of graphene quantum dots. The intensities are shown in the logarithmic scale and the frequency is shown in units of the frequency of the pulse, ω_0.

QDs, the frequency of the pulse is less than the band gaps. For the largest frequency of 1 rad/fs, i.e., the energy of 0.65 eV, the frequency of the pulse is greater than the band gap for all QDs considered here. For the intermediate frequency of 0.5 rad/fs, i.e., the energy of 0.33 eV, for small QDs, the frequency is less than the band gap, while for large QDs, the frequency is greater than the band gap. There are two main differences in radiation spectra for small and large frequencies: (i) at small frequency of the pulse, the cut off frequency has a stronger dependence on the QD radius compared to the case of a large frequency. (ii) at the large pulse frequency, the harmonic peaks become well pronounced, while such clear picture is not visible for a small pulse frequency. Also, due to the inversion symmetry of the system, only the odd harmonics are generated. The radiation spectra depend on the size of the system, i.e, on the QD radius, which affects both the cutoff frequency and the intensities of high harmonics. The intensities of the first high harmonics, i.e., the third, the fifth, and the seventh, are shown in Fig. 4.5 as a function of QD radius R. The results are shown for different frequencies of the pulse and different amplitudes. The general tendency is that with increasing the QD size the intensities of high harmonics decreases. Thus, for the sizes considered in the present paper, the maximum intensities of the low harmonics are mainly realized at the radius of 15 nm. But this dependence is not universal. For some parameters of the pulse, for example, for the third harmonics and the pulse amplitude of 0.1 V/Åand its frequency of 0.5 rad/fs, the maximum intensity is realized at the intermediate QD size, i.e., at $R = 20$ nm. Also, for the seventh harmonics and the field amplitude of 0.05 V/Å, see Fig. 4.5(i), the intensity of the harmonics increases with the radius.

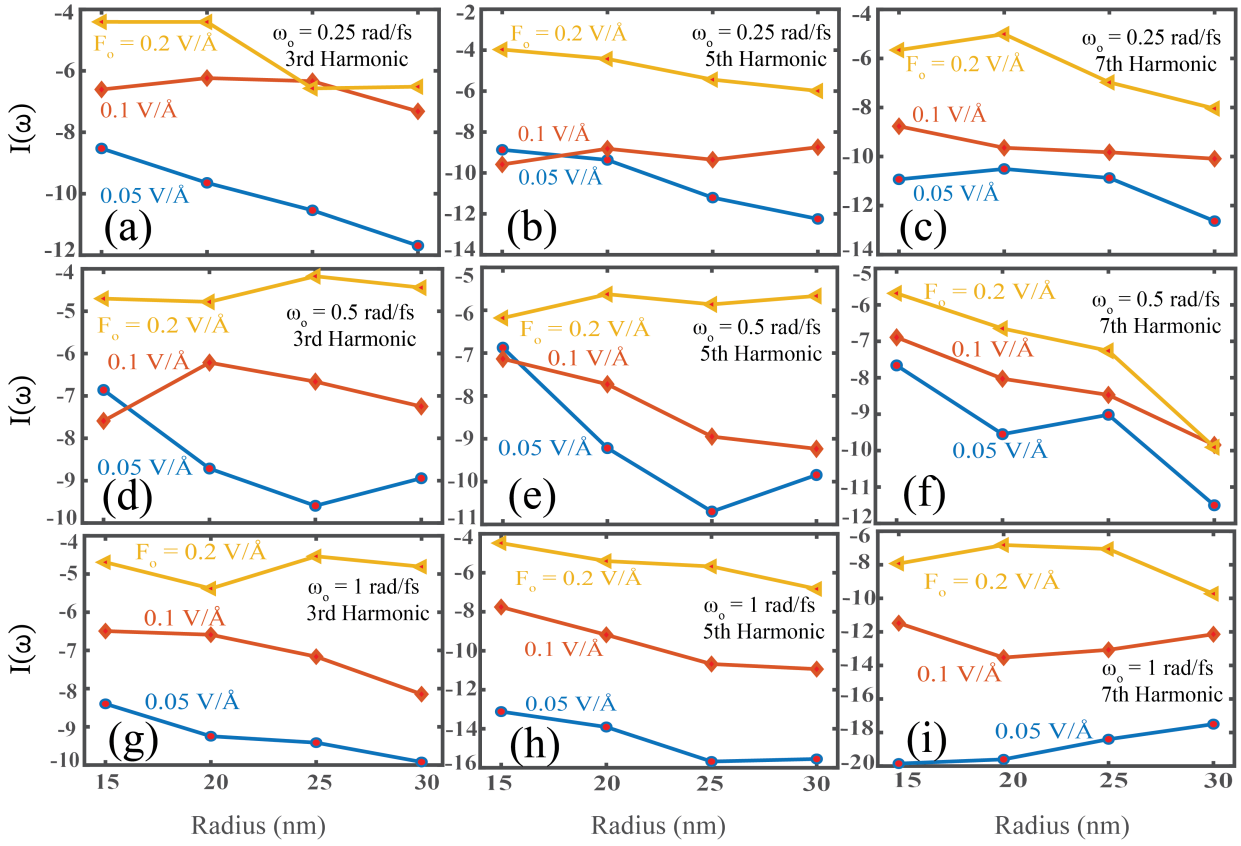

Figure 4.5 Intensities of high harmonics as a function of quantum dot radius. The data are shown for the first three harmonics: the third harmonic (a), (d), (g); the fifth harmonic (b), (e), (h); the seventh harmonic (c), (f), (i). The frequency of the pulse is marked in each panel. Different lines in each panel correspond to different pulse amplitudes, which are shown next to the corresponding lines.

Another important characteristic of the radiation spectra is the cutoff frequency. The dependence of the cutoff frequency on the QD size is shown in Fig. 4.6. The cutoff frequency monotonically increases with the QD radius, which is related to increasing the number of single-particle levels in QD systems. Also, as expected, the cutoff frequency increases with the amplitude of the pulse. As a function of the frequency, more harmonic modes are generated for low frequency pulses. For example, for the frequency of 0.25 rad/fs, see Fig. 4.6(c), up to 100 harmonics can be generated for the radius of 30 nm and the field amplitude of 0.2 V/Å, while for the frequency of 1 rad/fs, see Fig. 4.6(a), only 30 harmonics can be radiated. At the same time in terms of the maximum frequency or the cutoff energy, i.e., the maximum photon energy that can generated, these numbers are 25 rad/fs for the frequency of 0.25 rad/fs and 30 rad/fs for the pulse frequency of 1 rad/fs. Thus the higher frequency pulse has the larger cutoff energy. Another clear feature visible in Fig. 4.6 is that with increasing the field amplitude, the dependence of the cutoff frequency on the QD size becomes stronger, i.e., the slope of the dependence of the cutoff frequency on the QD radius increases with F_0. This can be attributed to the fact that with increasing the field amplitude, the energy interval within which the QD states are affected by the pulse increases, and for larger QDs, this will increase the number of excited QD states, which finally strongly affects the cutoff frequency.

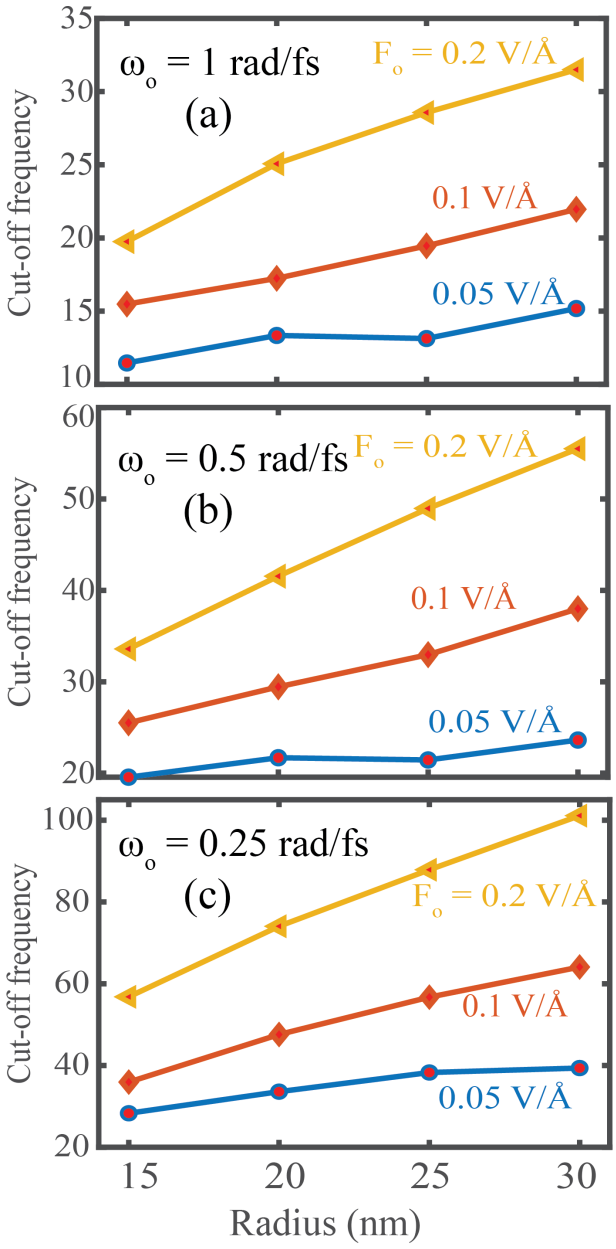

Figure 4.6 High harmonic cutoff as a function of the quantum dot radius. The frequency of the pulse is 1 rad/fs (a), 0.5 rad/fs (b, and 0.25 rad/fs (c). Different lines in each panel correspond to different field amplitudes, which are marked next to the corresponding lines.

4.4 Conclusion

The generation of high harmonics in low-dimensional QD systems interacting with a short optical pulse opens the possibility of controlling the nonlinear optical response of such systems by changing their size and shape. In this chapter, we addressed the problem of high harmonic generation in graphene QDs. The unique property of such QDs is that the band gap is entirely due to dimensional quantization without any bulk contribution, i.e., the graphene monolayer does not have any band gap. Thus, the band gap strongly depends on the QD size, and correspondingly the nonlinear optical response of graphene QDs is determined by their dimensions.

There are two main characteristics of the radiation spectra of QDs. The first one is the intensity of generated high harmonics and the second one is the cutoff frequency. Both of these characteristics can be controlled by the radius of a graphene QD. The intensities of the lowest generated harmonics mainly decrease with the QD size achieving their largest values for small QDs. At the same time, under some parameters of the pulse, the maximum intensities of high harmonics are realized at intermediate QD sizes. The cutoff frequency of the radiation spectrum has a more universal behavior. It monotonically increases with the QD size and the sensitivity of the cutoff frequency to the QD size increases with the pulse intensity.

We expect that the results obtained above that are related to the dependencies of the intensities of high harmonics and the cutoff frequency on the QD size will be similar for other shapes of graphene QDs.

CHAPTER 5

Generation of High Harmonics in a Graphene Quantum Dot Exhibiting Broken Time-Reversal Symmetry

5.1 Introduction

One of the many unique features of graphene systems is its unique optical, and transport properties. The symmetries, such as time reversal symmetry and inversion symmetry profoundly influence these features in a graphene system. The inversion symmetry in the system protects the low-energy relativistic dispersion of the Dirac type while the time reversal sym-

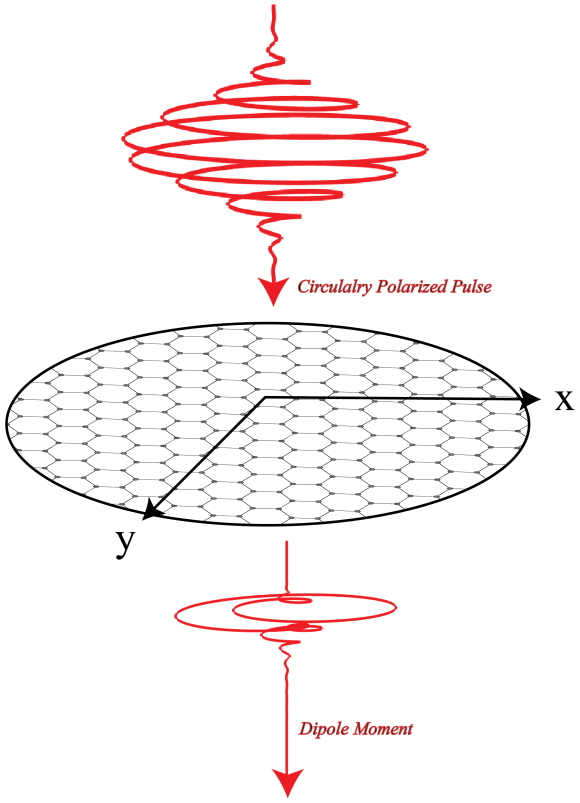

Figure 5.1 Schematic Representation of a Graphene Quantum Disk Interacting with Circulalry polarized Light and the Dipole moment as a result of interaction between QD and Ultrafast Pulse.

metry manifests itself in the form of degeneracy of K and K' valleys in a 2-dimensional crystal structure.

As mentioned in the previous chapters, to manipulate the inversion symmetry breaking phenomena, we used a unique approach of considering a quantum flake in an infinite potential of cylindrical form as compared to other methods such as applied electric field or substrate potential. Similarly, the time reversal symmetry is discussed in Chapter 3 in detail, circularly polarized light can break the time reversal symmetry of the graphene system.

In this chapter, we will discuss the phenomena of High Harmonic generation in graphene quantum dots with broken inversion symmetry. A circularly polarized light is used to influence the low energy electrons near the valleys of graphene quantum dots, causing nondegenerate valley polarization. This unique perturbation to electron eigenstates will generate an elliptically polarized dipole moment. A schematic diagram of a circularly polarized pulse producing a dipole moment which shows the fluctuation as well is shown in Fig. 5.1.

To study the energy spectrum of graphene QD of the shape of a disk we used the Dirac effective model, Eq. 2.1, and the energy eigenvalue equation is the same as Eq. 4.4. The energy spectrum of an unperturbed system can be seen in Fig. 4.2. As usual, the energy system exhibits quantized characteristics, while the K and K' valleys are mirror images of each other with a finite bandgap exhibiting typical behavior of broken inversion symmetry. The bandgap decreases with an increase in the size of the QD. The ultrafast optical pulse used to study the HHG is of cosine and sine form:

$$F_x(t) = F_{0,x} e^{-(t/\tau)^2} \cos(\omega_0 t), \tag{5.1}$$

$$F_y(t) = F_{0,y} e^{-(t/\tau)^2} \sin(\omega_0 t), \tag{5.2}$$

5.2 Results and Discussion

The radiation spectrum of graphene quantum dots is characterized primarily by cut-off frequency and the intensities of high harmonics. One way to analyze the transition of High Harmonics generated (HHG) from a linearly polarized pulse to a HHG as a result of QD shined by a circularly polarized laser pulse is introducing a parameter α such that it allows us to observe the transition of radiation spectrum from linear to elliptically polarized pulse by the following equation.

$$\alpha = F_{0,y}/F_{0,x} \tag{5.3}$$

The pulse amplitudes follow;

$$F_{0,x}^2 + F_{0,y}^2 = (F_0)^2 \tag{5.4}$$

Utilizing these mathematical expressions, we can methodically vary the parameter α within the range [0,1], facilitating an analysis of the transition in optical response from a linearly polarized pulse to a complete circularly polarized pulse.

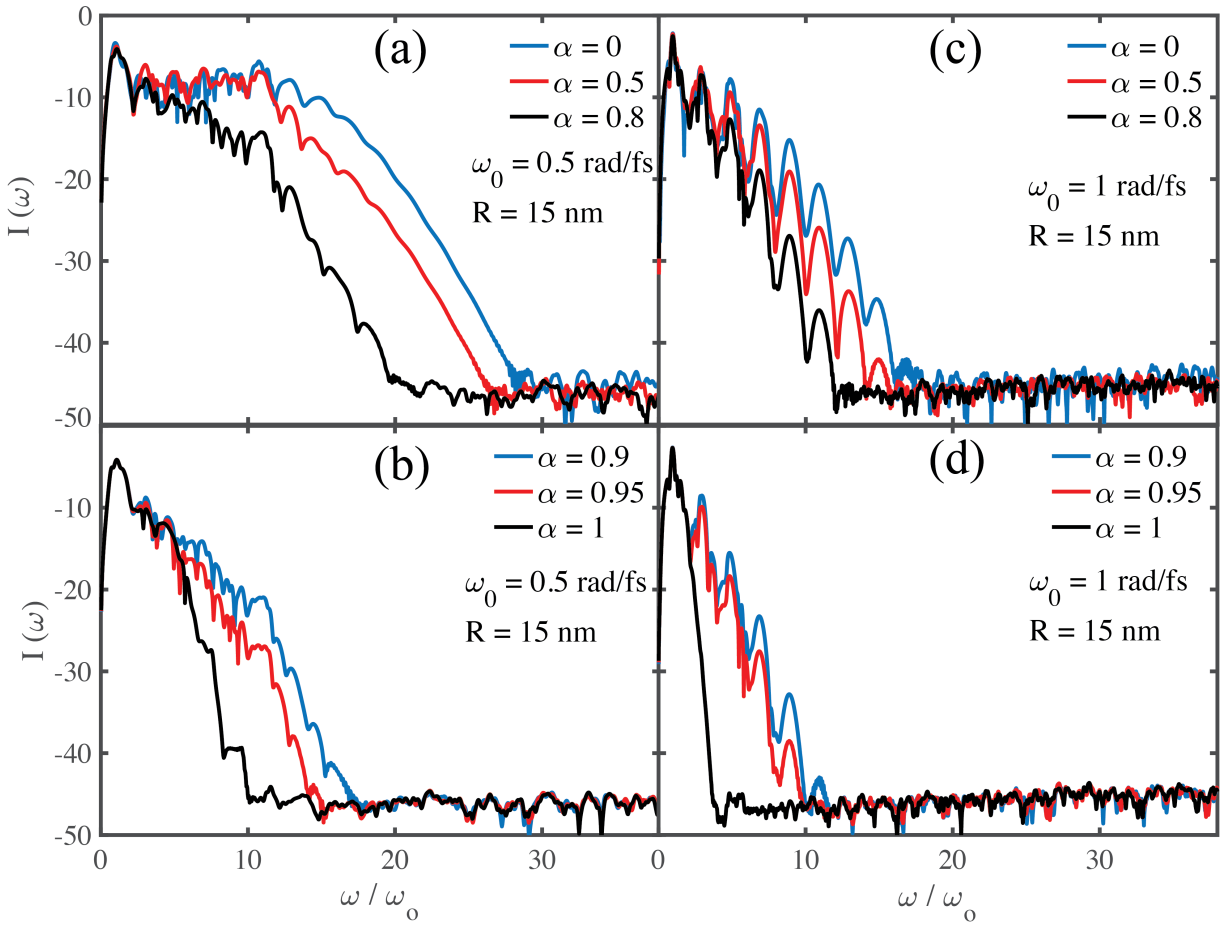

Figure 5.2 Radiation spectra of graphene QD. The frequency and size of QD are mentioned in each panel. Each line of the panel corresponds to a different ellipticity of the incident laser pulse. The vertical axis shows the intensities on a logarithmic scale, and frequencies are shown in units of frequency of the incident pulse.

In Fig. 5.2, the generated spectral profiles are shown in correspondence with varying ellipticities of the incident ultrafast laser pulses. The figure describes the spectral characteristics associated with laser pulses possessing frequencies of 1 rad/fs and 0.5 rad/fs, the interrelationship between ellipticity and the resultant spectral behaviors. A visible trend in Figure 1 is the decrement in the cutoff frequency with the increment in the ellipticity of the incident pulse.

The incident frequency of 0.5 rad/fs corresponds to an energy of 0.32 eV, which is lower than the bandgap energy of 0.57 eV associated with the quantum dot (QD) of size 15 nm. Conversely, the frequency of 1 rad/fs translates to an energy of 0.65 eV, which surpasses the bandgap energy of the QD.

A significant distinction between the radiation spectra of the QD is the dependency of harmonic peaks on the frequency of the applied pulse. In scenarios where a smaller frequency is applied, the radiation spectra exhibit a more plateaued trend. However, with the higher frequency of 0.65 eV, the harmonic peaks manifest with more prominent peaks and exhibit a pattern of decreasing intensities. The principle of inversion symmetry substantiates the emergence of solely odd harmonic peaks, thereby lending insight into the underlying physics of the spectral behavior as shown in Fig. 5.2. The pattern with which ellipticity, incident frequency, and high harmonic peaks interact shows the detailed changes in the radiation spectra of the QDs can be used on different parameters of perturbation.

The radiation spectra of QDs due to a linearly polarized light has a significant impact on the intensities of high harmonic for various sizes of QDs

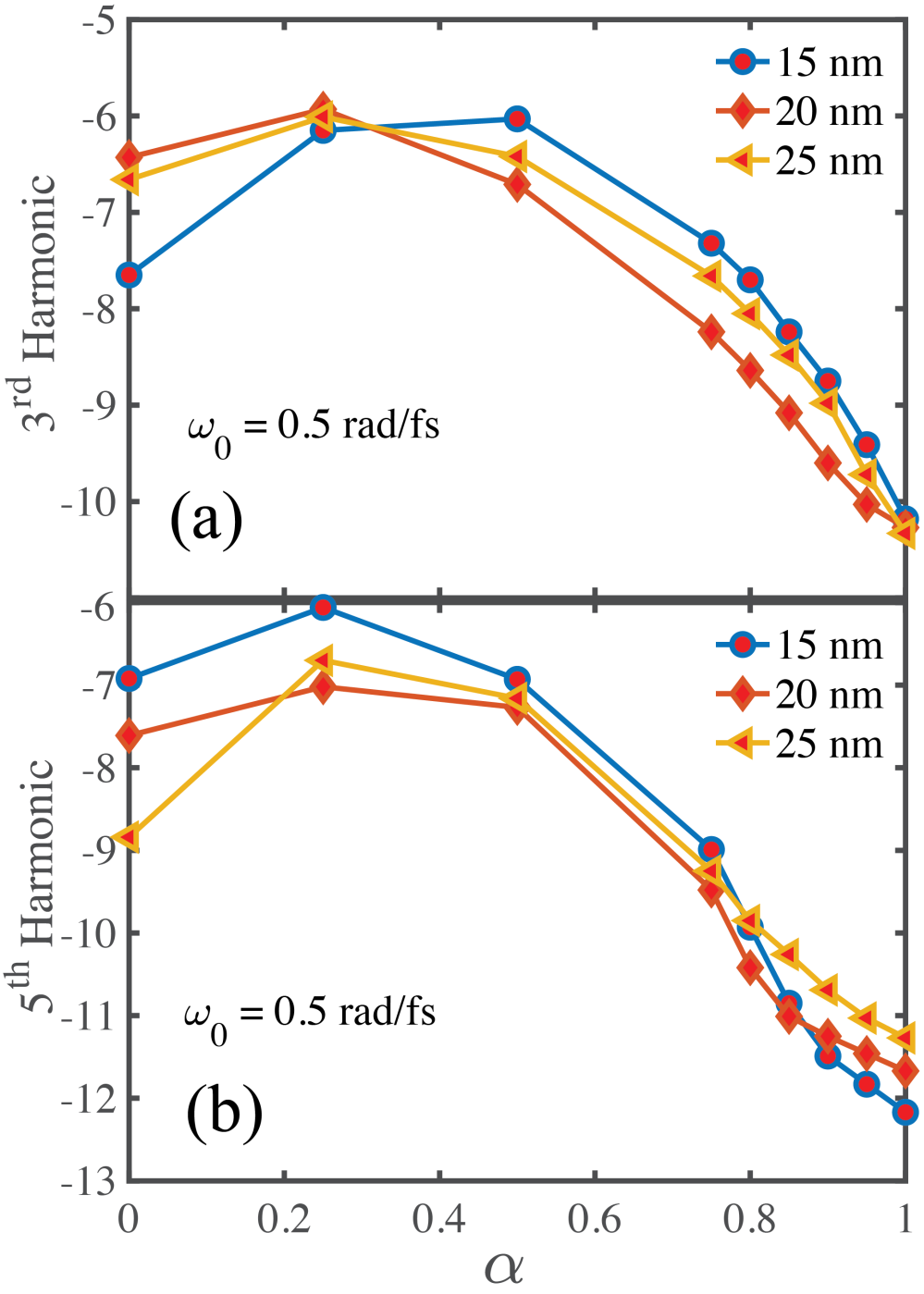

Figure 5.3 Intensities of (a) third and (b) fifth harmonics as a function of ellipticity α for three radii studied. The frequency of the applied pulse is mentioned in the panels.

as mentioned in Chapter 4. Fig. 5.3 depicts the third and fifth harmonics in relation to the ellipticity of the applied laser pulse.

We use the laser pulse of frequency 0.5 rad/fs, for an ellipticity parameter of $\alpha = 0$ (linearly polarized pulse), there is a monotonic increasing relationship between the intensities of third and fifth harmonics and the size of QD. The Larger QDs have more energy levels within the [-2,2] eV range, leading to an increase in the electron transitions.

Fig. 5.3(a) and 5.3(b) show that the third and fifth harmonics have a parabolic relation with pulse ellipticity. The peak intensities for both harmonics reach a maximum value at $\alpha = 0.25$. This highlights the role of ellipticity in adjusting high harmonic intensities.

For higher α values, the intensities tend to align with the cutoff frequency trend. This similarity reveals the mechanism affecting both harmonic intensities and the cutoff frequency. By analyzing these patterns, we gain deeper insight into the interplay between laser pulse ellipticity, QD size, and the resulting radiation spectra, enhancing our understanding of the phenomena of HHG.

The dipole moment is calculated from the expression 2.11 since we have used the circularly polarized pulse Eq. 5.1, and 5.2, the optical response in terms of dipole moment also carries an elliptical behavior. Fig. 5.4 shows the ellipticity $\alpha_{I(\omega)}$ for the third and fifth harmonic as a function of ellipticity of applied ultrafast laser pulse α_{in}. Initially, when $\alpha_{in} = 0$, i.e., the incident pulse is linearly polarized, the dipole moment shows a linear behavior as well, this has already been discussed in the previous chapter. For α_{in} values between 0.25 to 0.75 the ellipticity of output radiation polarized in a way that the y-component is greater than the

x-component, i.e., $\alpha_{I(\omega)} > 1$, see Fig. 5.5, reaching the maximum value of approximately 3. The dipole moment of QD is most sensitive in this range, making this plot a distinct peak or region of high intensity, emphasizing the pivotal role of pulse ellipticity. In the region of higher values of α_{in}, i.e., 0.75 and above, the ellipticity of the dipole moment shows a nonresponsive behavior, resulting in a circularly polarized dipole moment with $\alpha_{I(\omega)} = 1$. The general trend of the plot shows how the QD's dipole moment responds to varying incident pulse ellipticities. An initial upward trend indicates an increasing sensitivity of the QD as the pulse ellipticity increases, while a downward trend could signify diminishing returns or saturation effects.

The relationship between cut-off frequency, ellipticity, and the frequency of the applied laser pulse is an important aspect of the study, as shown in Fig. 5.6. The dependencies of the cutoff frequencies are examined for increasing values of ellipticity, for two specified frequencies, $\omega_0 = 1$ and 0.5 rad/fs. The graphical representation in Fig. 5.6 illustrates these dependencies, through a clearer understanding of the nonlinear dynamics. At $\alpha = 0$, the laser pulse manifests linear polarization, which generates a conduction band population distribution across both the K and K' valleys. This distribution results in a maximal number of high harmonics, thereby showcasing the consequential impact of linear polarization on harmonic generation. However, as the values of α increase to 0.75 or surpass this threshold, a sharp decline in the cutoff frequency trend is observed. As there is a gradual increment in the value of α, the cutoff frequency mostly remains stable, displaying no significant dependencies.

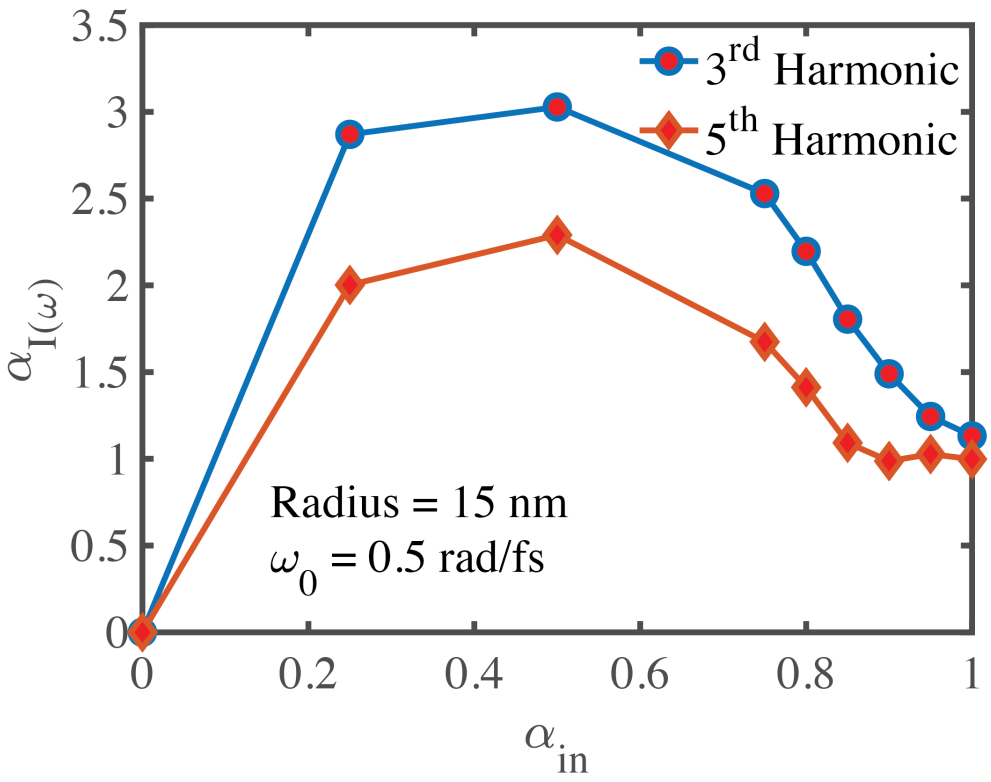

Figure 5.4 Ellipticity of Dipole moment at the third and fifth harmonic peak as a function of ellipticity of applied pulse. The radius of the QD and frequency of the applied pulse are mentioned in the plot.

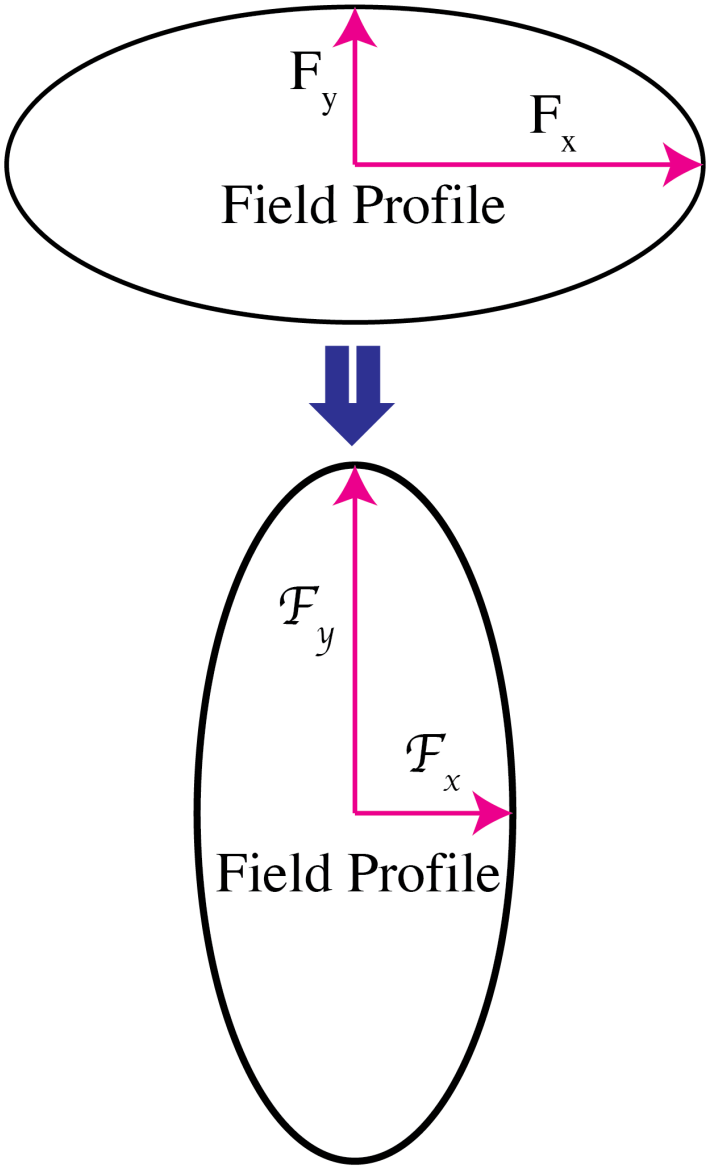

Figure 5.5 Schematic Diagram of an elliptically polarized ultrafast laser pulse and the resultant Elliptically Polarized Dipole moment in an opposite direction between the range $\alpha = 0.2 - 0.75$.

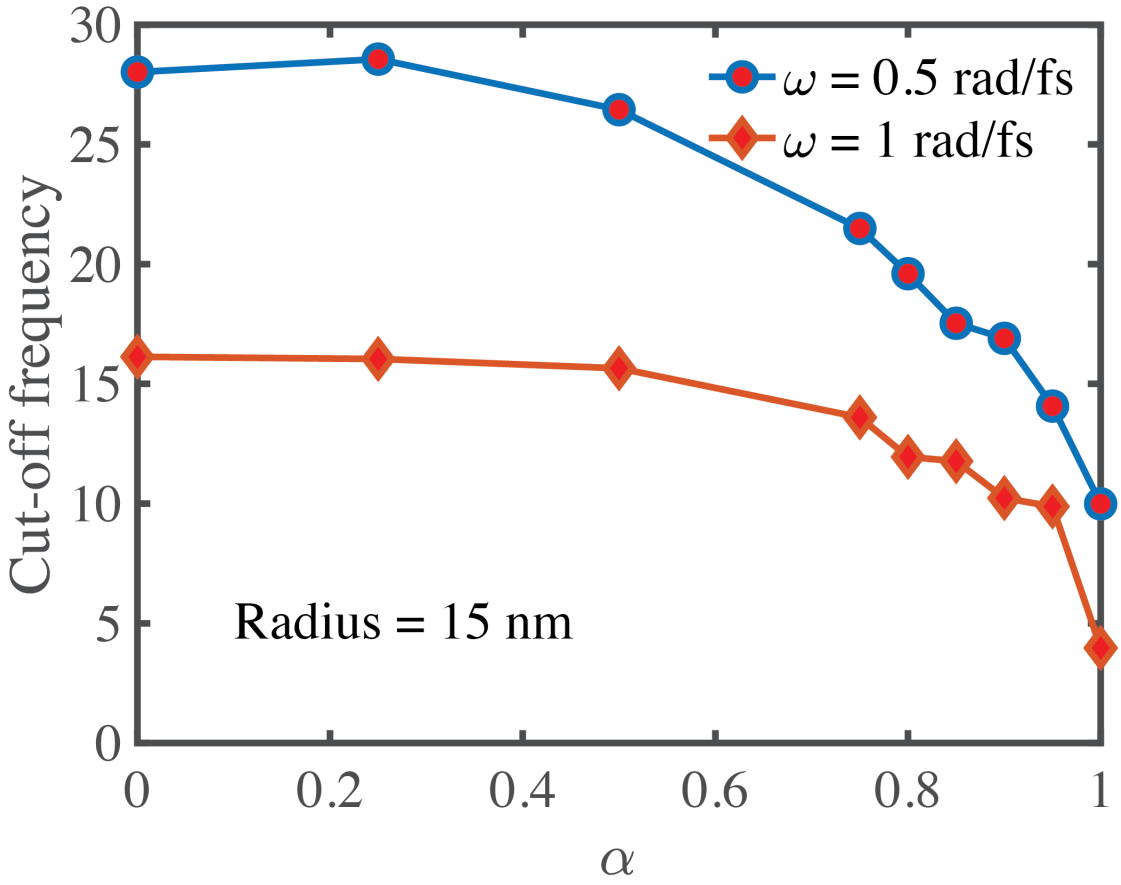

Figure 5.6 High Harmonic cutoff as a function of ellipticity α of the applied pulse. Two lines in the panel correspond to ω_0 0.5 rad/fs and 1 rad/fs.

The reason for suppressed cutoff frequency is the continuous rotational symmetry of the whole system (i.e., circular shape). The relationship between the decreasing cutoff frequency value and the shape of the nanosystem can be used for the conceptualization and development of devices of different shapes and dimensions. Therefore adding the scope of tuneable quantum optical device engineering and potentially advancing the frontier of knowledge in this domain.

Moreover, an interesting observation is that for a frequency of 0.5 rad/fs, the cut-off frequency is nearly twice that at 1 rad/fs, as shown throughout the trend in Fig. 5.6. At higher frequency, the system exhibits resonance and behaves like a two-state system. This observation underpins the direct correlation between the lower frequency of the applied pulse increased transitions to the CB states and the enhanced high harmonic generation. The significant role played by the frequency in modulating the spectral characteristics and high harmonic responses.

In the case of linear polarization laser pulse, a notable trend is observed in the cutoff energy for the radiation spectra, increasing monotonically with the increase in the quantum dot (QD) radius, as illustrated in Fig. 5.7. At an ellipticity parameter of $\alpha = 0$, the generated high harmonic modes for a QD radius of 25 nm approximates to 38. In comparison, a QD with the smallest radius of 15 nm generates a harmonic count of 28. This observation shows the substantial amplification of 78% in the harmonic count to a 36% increase in the geometric area of the QDs.

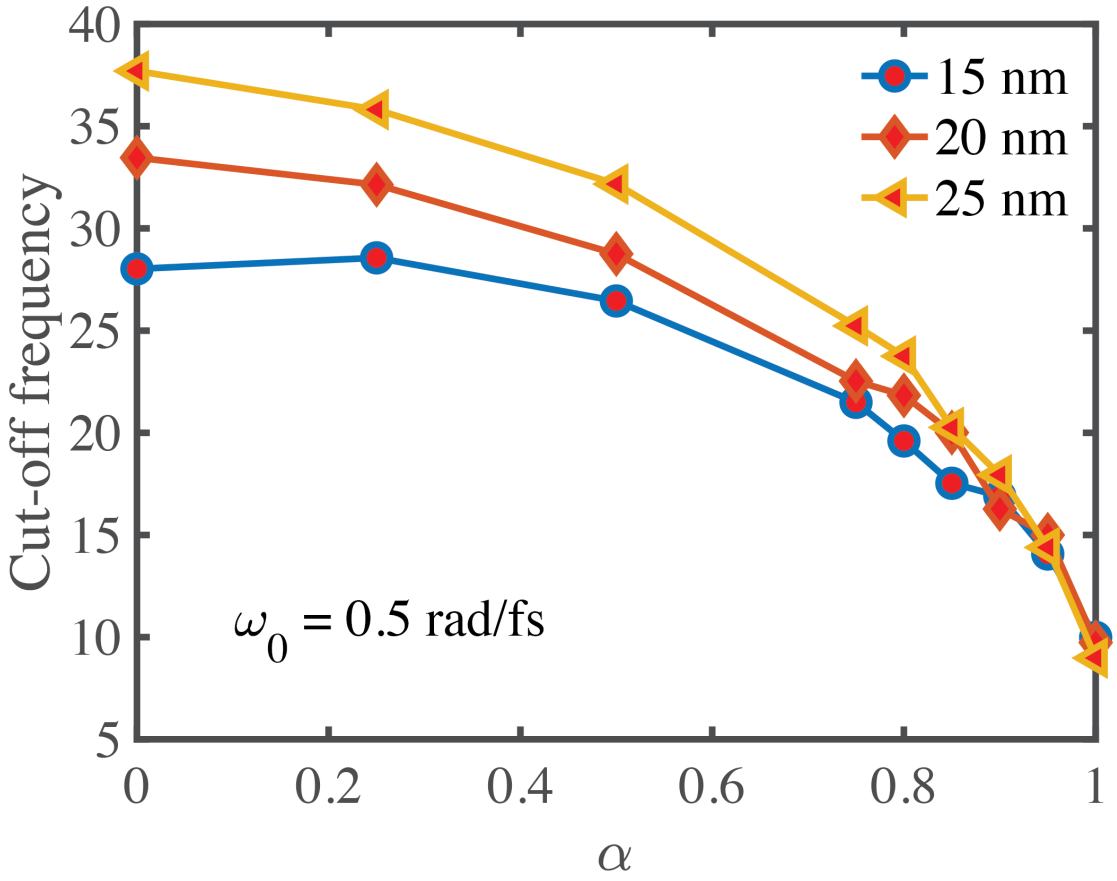

Figure 5.7 The cutoff frequency as a function of ellipticity parameter (α). Each line within the panel represents distinct radius values of the quantum dot (QD). The frequency of the applied pulse is denoted within the panel

As the ellipticity of the pulse increases to the threshold value of 0.75 and surpasses it, the cutoff frequency lines show a convergence trend to a particular point across all calculated radius values. This behavior shows that the cutoff frequency exhibits independence from the size of the QD at an ellipticity parameter of $\alpha = 1$, signifying a condition of complete circular polarization of the pulse. This observation unravels an important understanding of the relation between the ellipticity of applied pulse and the size of QD, and its impact on cutoff frequency, i.e., the cutoff frequency is independent of the size of the QD if a circularly polarized light is used. This is again due to the continuous rotational symmetry of the QD.

CHAPTER 6
SUMMARY

In this dissertation, we investigate the ultrafast non-linear dynamical behaviors of finite graphene structures, specifically focusing on two distinct geometries: nanorings and disk-shaped quantum dots.

Initially, we characterize the nanoring by the Dirac effective model, given its suitability as a region-specific analytical framework. Our primary emphasis is on the low-energy electronic states proximate to the K and K' valleys. A circularly polarized light is shined on the nanoring, leading to the disruption of time-reversal symmetry, a phenomenon to which pristine graphene is intrinsically insensitive. As a consequence of broken time reversal, the population of electrons in the conduction band region of valleys is non-degenerate. This non-degenerate behavior of valleys can be controlled by changing the laser parameters such as amplitude and pulse duration. While the population of the conduction band region augments in correlation with the enhancement of field parameters, there is discernible evidence of a non-degenerate valley population in the graphene quantum ring. After the establishment of this idea that the broken time reversal symmetry causes valley polarization, the final results of this study were analyzed for different inner and outer radii with increasing field amplitude. The valley polarization plots were interpolated for a smaller field amplitude. These interpolated functions facilitate the precise determination of valley polarization in the system, obviating the need for resource-intensive computations. Consequently, this offers a direct methodology for designing nanodevices to achieve specific valley polarizations.

We study the behavior of non-linear optical dynamics of a disk-shaped graphene nanoflake. A linearly polarized optical pulse, characterized by a cosine waveform, is employed to perturb the system, leading to the electron population transition into the valley regions of the conduction band. The temporally variant coefficients of electron wave functions encapsulate the requisite information for determining the dipole moment of a graphene quantum dot. The emission spectrum, derived from the Fourier transformation of the time-domain dipole moment, exhibits two primary characteristics: the cutoff frequency and the intensity of harmonics generated due to the influence of the ultrafast pulse. These two characteristics of the emission spectrum, the intensity of generated harmonics, and the cutoff frequency display a dependence on the quantum dot size. Harmonic intensities exhibit a dual behavior: the intensities of the lower harmonics diminish with increasing quantum dot size, attaining their maximal values for smaller quantum dots, while under certain pulse parameters, peak intensities of high harmonics manifest at intermediate sizes. Interestingly, the cutoff frequency demonstrates a consistent trend, increasing monotonically with quantum dot size, with its sensitivity increasing alongside pulse intensity. It is concluded that these observations concerning harmonic intensities and cutoff frequency in relation to quantum dot size may extend to other geometries of graphene-based devices.

Furthermore, we study the optical response of disk-shaped graphene QD, while changing the ellipticity of laser pulse from complete linear polarization to circular polarization. The two important characteristics of radiation spectra were analyzed while the polarization of light makes the transition from linear to completely circular. The cutoff frequency of QD

suppresses under the influence of circularly polarized light due to the continuous rotational symmetry of the system, this suppression of cutoff frequency results in its independence from the radius of the quantum dot. However, different values of cutoff frequency at different ellipticity suggest a tunable behavior in the optical response of quantum dots. The intensities of harmonics, which have monotonic dependence on the quantum dot size for a linearly polarized pulse also shows a sharp decline when the ellipticity of the laser pulse is close to the circular polarization value. This behavior similar to cutoff frequency also results from the interplay of rotational symmetry and polarization of incident pulse.

Further investigation into various graphene configurations, for example, graphene nanoribbons, and complex structures could reveal more interesting characteristics of ultrafast nonlinear dynamics on graphene-based systems. Furthermore, the recent synthesis of $MoSi_2N_4$ and WSi_2N_4 monolayers has indicated the inception of a novel class of two-dimensional (2D) MA_2Z_4 materials, these materials vary from non-magnetic, anti-ferromagnetic, to ferromagnetic semiconductors, half-metals, and metals. The study of nonlinear dynamics in such materials under the influence of ultrafast laser pulse can open up near frontiers in valleytronics and high harmonic generation, as the bandgap of these materials is tuneable due to broken inversion symmetry and external electric field.

Moreover, Investigating the response of these graphene nanostructures to various laser fields, beyond the polarized pulse currently employed, and studying the correlation between mechanical and optical properties, such as the effects of strain on the non-linear optical responses of graphene structures, could open up novel perspectives in material science.

Appendices

A Appendix A

Listing 1 Graphene quantum dot solver

```
% ========================================
% Graphene Quantum Ring Eigenvalue Solver
%
% This script numerically solves the eigenvalue equation of a
   graphene
% quantum ring using the Dirac effective model. The outer
   radius is fixed,
% and solutions are obtained for different inner radius values.
%
% The bisection method is employed to find solutions where the
   function
% changes its sign. Solutions exhibiting asymptotic behavior
   are filtered
% out to retain only physical solutions of the equation.
% ============================================
```

```
% ------ Clear workspace and close figures ------
clear all;
close all;


% ========================= Parameters ==============
% Define the parameters needed for the calculations.


h = 0.65821;        % Reduced Planck constant (in eV fs)
gamma = 3.03;       % The nearest neighbor hopping integral (in
   eV)
Rin = 5;            % Rin  - Inner radius of the quantum ring (
   in nm)
Rout = 15;          % Rout - Outer radius of the quantum ring (
   in nm)
m = -41/2:1:41/2;   % Magnetic quantum number
T = 1e3;            % Total number of input points for eigen
   function
S = 15;             % Number of solutions this code will go
   through
```

```
% ====================== Calculations ======================
% Perform the calculations for different inner and outer radius
    values.

% Initialize a parallel processing loop over different inner
   and outer radius values

Energy_k = zeros(2*S,length(m));
for i = 1:length(Rin)
    Ri = Rin(i);  % Current inner radius value
    % Calculate solutions and store them in E_k
    E_k = Solution(S, Ri, Rout, gamma, m, T);
    Energy_k(:,:,i) = E_k;  % Store the current solutions in
       the Energy_k matrix
end

% Save the calculated energy values for the K valley
ENERGY_K_valley = Energy_k;
save('ENERGY_K_valley');
```

```
% ====================== Function Definitions ==========
function Energy_k = Solution(S, rin, rout, gamma, m, T)
    % Solution Function
    %
    % Computes the energy levels near the K-Valley of a
       Graphene Quantum Ring,
    % considering the asymptotic solutions and zero crossings.
    %
    % Inputs:
    %   S      - Number of solutions this code will go through.
    %   rin    - Inner radius (in nm)
    %   rout   - Outer radius (in nm)
    %   gamma  - The nearest neighbor hopping integral
    %   m      - Magnetic quantum number
    %   T      - Total Number of input points for Eigen
       function
    %
    % Output:
    %   Energy_k - Calculated energy levels (in eV)

    % Initialize Position and Negative arrays
```

```
Pos = zeros(S, length(m));
Neg = zeros(S, length(m));

% Loop over each magnetic quantum number to determine the
   Asymptotic solutions.
for i = 1:length(m)
    MM = m(i);
     [pos,~]=asymptotes(rin./rout,MM,T);
        if  length(Pos(:,i)) == length(pos)
        Pos(:,i) = flip(pos);                    %epsilon for
            conduction band
    elseif length(Pos(:,i)) -length(pos) >0
        a1 = length(Pos(:,i)) - length(pos);
        b1 = zeros(a1,1);
        pos1 = [pos;b1];
        Pos(:,i) = flip(pos1);                   %epsilon for
            conduction band
        else
        if length(Pos(:,i)) -length(pos) <0
        a3 = length(pos)- length(Pos(:,i));
        pos2 = pos(1:end-a3);
```

```
    Pos(:,i) = flip(pos2) ;                    %epsilon for
        conduction band
    end
    end
 [~,neg]=asymptotes(rin./rout,MM,T);
    if  length(Neg(:,i)) == length(neg)
    Neg(:,i) = (neg);                          %epsilon for
        valence band
elseif  length(Neg(:,i)) - length(neg) >0
    a2 = length(Neg(:,i)) - length(neg);
    b2 = zeros(a2,1);
    neg1 = [neg;b2];
    Neg(:,i) = (neg1);                         %epsilon for
        valence band
else
    if length(Neg(:,i)) - length(neg) < 0
    a4 =  length(neg) - length(Neg(:,i));
    neg2 = neg(1:end-a4);
    Neg(:,i) = (neg2);                         %epsilon for
        valence band
    end
```

```
        end
end


% Merge positive and negative asymptotes
Asymptotes = [Pos; Neg];
e_C = zeros(S, length(m));
e_V = zeros(S, length(m));


% Adjust array lengths for all solutions to be stored in
   one matrix.
for i = 1:length(m)
    MM = m(i);
     [E_c1,~]=zero_crossings(rin./rout,MM,T);
        if  length(e_C(:,i)) == length(E_c1)
        e_C(:,i) = flip(E_c1);                %epsilon for
           conduction band
    elseif length(e_C(:,i)) -length(E_c1) >0
        a5 = length(e_C(:,i)) - length(E_c1);
        b5 = zeros(a5,1);
        E_c = [E_c1;b5];
```

```
    e_C(:,i) = flip(E_c);                    %epsilon for
       conduction band
    else
    if length(e_C(:,i)) -length(E_c1) <0
    a6 = length(E_c1)- length(e_C(:,i));
    E_c = E_c1(1:end-a6);
    e_C(:,i) = flip(E_c) ;                   %epsilon for
       conduction band
    end
    end
 [~,E_v1]=zero_crossings(rin./rout,MM,T);
    if  length(e_V(:,i)) == length(E_v1)
    e_V(:,i) = (E_v1);                       %epsilon for
       valence band
elseif  length(e_V(:,i)) - length(E_v1) >0
    a7 = length(e_V(:,i)) - length(E_v1);
    b6 = zeros(a7,1);
    E_v = [E_v1;b6];
    e_V(:,i) = (E_v);                        %epsilon for
        valence band
else
```

```
        if length(e_V(:,i)) - length(E_v1) < 0
        a4 =  length(E_v1) - length(e_V(:,i));
        E_v = E_v1(1:end-a4);
        e_V(:,i) = (E_v);                          %epsilon
           for valence band
        end
        end
end


epsilon1 = [e_C; e_V];


% Filter out asymptotic solutions from the physical
   solutions.
[Rows, Cols] = size(epsilon1);
Epsilon1 = zeros(Rows, Cols);
for j = 1:Cols
    a = Asymptotes(:, j);
    b = epsilon1(:, j);
    b(ismember(b, a)) = 0;  % Replace asymptotic solutions
       with zero
```

```
        Epsilon1(:, j) = b;      % Epsilon is a unitless
           variable for energy.
    end

    % Convert unitless variable to energy in eV

    Energy_k = (Epsilon1 .* gamma ./ rout);
end

% ============= Function Definitions ================

function [pos, neg] = asymptotes(beta, M, T)
    % Asymptotes Function
    % This function finds the asymptotes of the energy levels
       in a Graphene
    % Quantum Ring by looking for zero-crossings in the energy
       eigenvalue equation.
    % Inputs:
    %   beta - Ratio of inner to outer radius
    %   M    - Magnetic quantum number
    %   T    - Total number of input points for Eigen function
```

```
%
% Outputs:
%   pos - Positive energy eigenvalues corresponding to K-
   Valley
%   neg - Negative energy eigenvalues corresponding to K-
   Valley

E2 = linspace(0, -50, T);
E1 = linspace(0, 50, T);
y1 = real(energies(beta, E1, M));
y2 = real(energies(beta, E2, M));

% Initialize zero-crossing counts for positive and negative
    energies in K-valley
kp1 = 1;
kn1 = 1;

for n = 1:T
    if n == T
        % Avoid exceeding the length of the array in (i+1)-
           th terms
```

```
    break
else
    % K-Valley - Positive energy
    a1p1 = y1(n);
    a2p1 = y1(n + 1);
    Pap1 = a2p1 * a1p1;  % Product of consecutive terms
        - positive energy - K-Valley

    % K-Valley - Negative energy
    a1n1 = y2(n);
    a2n1 = y2(n + 1);
    Pan1 = a1n1 * a2n1;  % Product of consecutive terms
        - negative energy - K-Valley

    % Selection of zeros of the energy eigenvalue
       equation by finding the zero crossings

    % K-Valley Positive eigenenergies
    if Pap1 < 0 && imag(a1p1) == 0 && imag(a2p1) == 0
        Energy_valuesp1(kp1, 1) = (E1(n) + E1(n + 1)) /
            2;  % Find energy eigenvalues
```

```
            kp1 = kp1 + 1;
        elseif Pap1 > 0
            Energy_valuesp1(kp1, 1) = 0;
            kp1 = kp1 + 1;
        end

        % K-Valley Negative eigenenergies
        if Pan1 < 0 && imag(a1n1) == 0 && imag(a2n1) == 0
            Energy_valuesn1(kn1, 1) = (E2(n) + E2(n + 1)) /
                2;  % Find energy eigenvalues
            kn1 = kn1 + 1;
        elseif Pan1 > 0
            Energy_valuesn1(kn1, 1) = 0;
            kn1 = kn1 + 1;
        end
    end
end

% Find band gap between corresponding energy levels of
   conduction and valance band
pos = nonzeros(Energy_valuesp1);
```

```
    neg = nonzeros(Energy_valuesn1);


    % Helper Function to Calculate the values of Denominator of
        EigenValue
    % Equation


function y = energies(beta, E, M)
    y = zeros(1, length(E));
    for j = 1:length(E)
        er = E(j);
        [Y] = deno(beta, er, M);
        y(j) = Y;
    end
end


% Helper Function to Calculate the Denominator of the Energy
   Eigenvalue Equation
function [Y] = deno(b, E, m)
    % Bessel function = besselj
    % Neumann function = bessely
```

```
    Y = (besselj(m + 1/2, b .* (E)) + besselj(m - 1/2, b .* (E)
       ));

end



end

% ================ Function Definitions =================

function [E_c, E_v] = zero_crossings(beta, M, T)
    % zero_crossings Function
    %
    % Computes all values of zero crossing of Eigenvalue
       Equation at given input parameters.
    %
    % Inputs:
    %   beta - Ratio of inner and outer Radius
    %   M    - Magnetic Quantum number
    %   T    - Total Number of input points for Eigen Equation
    %
```

```
% Outputs:
%   E_c - Solution in positive energy region
%   E_v - Solution in negative energy region

% Initialize Energy Ranges and Values
E2 = linspace(0, -50, T);
E1 = linspace(0, 50, T);
y1 = real(values(beta, E1, M));
y2 = real(values(beta, E2, M));

% Initialize zero-crossing counts for K-valley energies
kp1 = 1;
kn1 = 1;

for n = 1:T
    if n == T  % Avoid exceeding the length of the array
        break
    else
        % K-Valley - Positive Energy
        a1p1 = y1(n);
        a2p1 = y1(n + 1);
```

```
Pap1 = a2p1 * a1p1;  % Product of consecutive terms

% K-Valley - Negative Energy
a1n1 = y2(n);
a2n1 = y2(n + 1);
Pan1 = a1n1 * a2n1;  % Product of consecutive terms

% Select zeros of the energy eigenvalue equation by
    finding zero crossings

% K-Valley Positive Eigenenergies
if Pap1 < 0 && imag(a1p1) == 0 && imag(a2p1) == 0
    Energy_valuesp1(kp1, 1) = (E1(n) + E1(n + 1)) /
        2;  % Find energy eigenvalues
    kp1 = kp1 + 1;
end

% K-Valley Negative Eigenenergies
if Pan1 < 0 && imag(a1n1) == 0 && imag(a2n1) == 0
    Energy_valuesn1(kn1, 1) = (E2(n) + E2(n + 1)) /
        2;  % Find energy eigenvalues
```

```
            kn1 = kn1 + 1;
        end
    end
end

% Store the Corresponding Energy Levels of Conduction and
   Valance Band
E_c = Energy_valuesp1;
E_v = Energy_valuesn1;

% Nested Function to Compute the Values of the Eigenvalue
   Equation
function y = values(beta, E, M)
    y = zeros(1, length(E));
    for j = 1:length(E)
        er = E(j);
        [Y] = eigenequation(beta, er, M);
        y(j) = Y;
    end
end
```

```
    % Nested Eigen Equation Function
    function [Y] = eigenequation(b, E, m)
        % b - beta (Ratio of inner and outer Radius)
        % m - Magnetic Quantum number
        % E - Energy Level

        a = (-bessely(m + 1/2, b .* (E)) - bessely(m - 1/2, b
           .* (E))) ./ ...
            (besselj(m + 1/2, b .* (E)) + besselj(m - 1/2, b .*
                (E)));

        x1 = a .* besselj(m - 1/2, E);
        x2 = a .* besselj(m + 1/2, E);
        x3 = bessely(m + 1/2, E);
        x4 = bessely(m - 1/2, E);

        Y = x1 + x2 + x3 + x4;
    end
end
```

B Appendix B

Listing 2 Fourier Transformation of Dipole moment

```
% Clearing workspace and command window
clear all
clc

% Starting timer to measure the execution time
tic

% Defining constants and parameters
omega = 1;
t = linspace(-100,200,5000);  % time vector
tau_relx = 15;  % relaxation time
w = '1';        % omega string for file naming
Fo = '05';      % Fo string for file naming
tau = '15';     % tau string for file naming
radius = '5';   % radius string for file naming

f_o = (str2double(Fo)/100);
```

```
w_o = (str2double(w)/1);


% Creating file and path strings for loading data
s1 = '_w_';
w_field = strcat(s1,w);
s2 = 'Fx_';
F_field = strcat(s2,Fo);
s3 = '_tau_';
tau_field = strcat(s3,tau);


name_kx = strcat('Dxk_r',radius,'_k_');
name_ky = strcat('Dyk_r',radius,'_k_');


type = '.mat';


File_kx_valley = strcat(name_kx,F_field,tau_field,w_field);
File_ky_valley = strcat(name_ky,F_field,tau_field,w_field);


path = 'C:\Users\Jawad\OneDrive␣-␣Georgia␣State␣University\
   Matlab␣Codes\graphene␣quantum␣rings\Harmonics\Disk\
   Disk_diff_radius\output\';
```

```
% Loading x and y dipole moment data
Dxt = load(strcat(path,File_kx_valley,type));
dxt = fieldnames(Dxt);
dxt = Dxt.(dxt{1});
xk = (dxt);

Dyt = load(strcat(path,File_ky_valley,type));
dyt = fieldnames(Dyt);
dyt = Dyt.(dyt{1});
yk = (dyt);

% Processing dipole moment data
x = 2.*xk;
Y = yk;

% Plotting x dipole moment versus time
figure(11)
plot(t,real(x),'LineWidth',2)
title(['F_o = ',num2str(f_o),',  \omega_f_i_e_l_d = ',num2str(
   w_o), ', \tau_f_i_e_l_d = ',tau])
```

```
legend('Without␣relaxation')

xlabel('time␣(fs)')

ylabel('d_x(t)')

xlim([t(1) t(end)])

ax = gca;

ax.FontSize = 15;

ax.FontWeight = 'bold';

ax.LineWidth = 2;


% Plotting y dipole moment versus time

figure(2)

plot(t,real(Y),'LineWidth',2)

title(['F_o␣=␣',num2str(f_o),',␣␣\omega_f_i_e_l_d␣=␣',num2str(

   w_o), ',␣\tau_f_i_e_l_d␣=␣',tau])

xlabel('time␣(fs)')

ylabel('d_y(t)')

xlim([t(1) t(end)])

ax = gca;

ax.FontSize = 15;

ax.FontWeight = 'bold';

ax.LineWidth = 2;
```

```
% Applying relaxation and differentiating x dipole moment
for i = 1:length(t)
    X(i) = x(i).*exp(-t(i)./tau_relx);
end
DxDt = diff(X)./diff(t);
F_w = fft(DxDt);

% Fourier transforming the differentiated x dipole moment
L = length(t);
Y = F_w;
Fs = length(t)/(t(end) - t(1));
P2 = abs((Y)/L);
P1 = P2(1:L/2+1);
P1(2:end-1) = P1(2:end-1);

f = 2*pi*Fs*(0:(L/2))/L;
D_w = (abs(P1.*(t(end) - t(1))).^2).*(f.^2);

% Plotting the Fourier transformed and differentiated x dipole
   moment
```

```
figure(33)
plot((f./omega),log(D_w./((pi*str2num(radius)^2)).^2),'
   LineWidth',3)
title(['\omega_f_i_e_l_d␣=␣',num2str(w_o), '␣F_o␣=␣',num2str(
   f_o), '␣V/  ']) 
xlabel('\omega␣/␣\omega_f_x')
ylabel('|D_x␣(w)|^2␣\omega^2␣/␣Area^2')
legend(['R␣=␣',num2str(radius), '␣nm'])
ax = gca;
ax.FontSize = 20;
ax.FontWeight = 'bold';
ax.LineWidth = 3;


% Plotting x dipole moment with relaxation versus time
figure(34)
plot(t,real(X),'LineWidth',3)
title(['\omega_f_i_e_l_d␣=␣',num2str(w_o), '␣F_o␣=␣',num2str(
   f_o), '␣V/  ']) 
legend(['R␣=␣',num2str(radius), '␣nm'])
xlabel('time␣(fs)')
ylabel('d_x(t)')
```

```
xlim([-50 50])

ax = gca;

ax.FontSize = 20;

ax.FontWeight = 'bold';

ax.LineWidth = 3;



% Stopping timer and displaying the elapsed time

toc
```

REFERENCES

[1] S Azar Oliaei Motlagh, Fatemeh Nematollahi, Aranyo Mitra, Ahmal Jawad Zafar, Vadym Apalkov, and Mark I Stockman. Ultrafast optical currents in gapped graphene. *Journal of Physics: Condensed Matter*, 32(6):065305, 2019.

[2] S Azar Oliaei Motlagh and Vadym Apalkov. Absorption properties of graphene quantum dots under ultrashort optical pulses. *Physical Review B*, 104(4):045421, 2021.

[3] Ferenc Krausz and Mark I Stockman. Attosecond metrology: from electron capture to future signal processing. *Nature Photonics*, 8(3):205–213, 2014.

[4] Hanieh Fattahi, Helena G Barros, Martin Gorjan, Thomas Nubbemeyer, Bidoor Alsaif, Catherine Y Teisset, Marcel Schultze, Stephan Prinz, Matthias Haefner, Moritz Ueffing, et al. Third-generation femtosecond technology. *Optica*, 1(1):45–63, 2014.

[5] Wolfgang Kaiser and David H Auston. *Ultrashort laser pulses: generation and applications*. Springer, 1993.

[6] Ahmed H Zewail. Femtochemistry: Atomic-scale dynamics of the chemical bond. *The Journal of Physical Chemistry A*, 104(24):5660–5694, 2000.

[7] Eleftherios Goulielmakis, Vladislav S Yakovlev, Adrian L Cavalieri, Matthias Uiberacker, Volodymyr Pervak, A Apolonski, Reinhard Kienberger, Ulf Kleineberg, and Ferenc Krausz. Attosecond control and measurement: lightwave electronics. *Science*, 317(5839):769–775, 2007.

[8] Vladislav S Yakovlev, Stanislav Yu Kruchinin, Tim Paasch-Colberg, Mark I Stockman,

and Ferenc Krausz. Ultrafast control of strong-field electron dynamics in solids. *Ultrafast Dynamics Driven by Intense Light Pulses: From Atoms to Solids, from Lasers to Intense X-rays*, pages 295–315, 2016.

[9] Hamed Koochaki Kelardeh, Vadym Apalkov, and Mark I Stockman. Graphene in ultrafast and superstrong laser fields. *Physical Review B*, 91(4):045439, 2015.

[10] THAT GENERATE ATTOSECOND PULSES OF LIGHT. For experimental methods that generate attosecond pulses of light for the study of electron dynamics in matter. 2023.

[11] Philip Richard Wallace. The band theory of graphite. *Physical review*, 71(9):622, 1947.

[12] Kostya S Novoselov, Andre K Geim, Sergei V Morozov, De-eng Jiang, Yanshui Zhang, Sergey V Dubonos, Irina V Grigorieva, and Alexandr A Firsov. Electric field effect in atomically thin carbon films. *science*, 306(5696):666–669, 2004.

[13] AH Castro Neto, Francisco Guinea, Nuno MR Peres, Kostya S Novoselov, and Andre K Geim. The electronic properties of graphene. *Reviews of modern physics*, 81(1):109, 2009.

[14] S Das Sarma, Shaffique Adam, EH Hwang, and Enrico Rossi. Electronic transport in two-dimensional graphene. *Reviews of modern physics*, 83(2):407, 2011.

[15] Di Xiao, Ming-Che Chang, and Qian Niu. Berry phase effects on electronic properties. *Reviews of modern physics*, 82(3):1959, 2010.

[16] John R Schaibley, Hongyi Yu, Genevieve Clark, Pasqual Rivera, Jason S Ross, Kyle L Seyler, Wang Yao, and Xiaodong Xu. Valleytronics in 2d materials. *Nature Reviews*

Materials, 1(11):1–15, 2016.

[17] John Schaibley. Valleytronics in 2d semiconductors. In *2D Materials for Photonic and Optoelectronic Applications*, pages 281–302. Elsevier, 2020.

[18] Steven A Vitale, Daniel Nezich, Joseph O Varghese, Philip Kim, Nuh Gedik, Pablo Jarillo-Herrero, Di Xiao, and Mordechai Rothschild. Valleytronics: opportunities, challenges, and paths forward. *Small*, 14(38):1801483, 2018.

[19] Hamed Koochaki Kelardeh, Vadym Apalkov, and Mark I Stockman. Attosecond strong-field interferometry in graphene: Chirality, singularity, and berry phase. *Physical Review B*, 93(15):155434, 2016.

[20] S Azar Oliaei Motlagh, Jhih-Sheng Wu, Vadym Apalkov, and Mark I Stockman. Femtosecond valley polarization and topological resonances in transition metal dichalcogenides. *Physical Review B*, 98(8):081406, 2018.

[21] S Azar Oliaei Motlagh, Fatemeh Nematollahi, Vadym Apalkov, and Mark I Stockman. Topological resonance and single-optical-cycle valley polarization in gapped graphene. *Physical Review B*, 100(11):115431, 2019.

[22] Krishna Rana Magar, S Azar Oliaei Motlagh, and Vadym Apalkov. Topological resonance in graphene-like materials. *Journal of Physics: Condensed Matter*, 34(37):375301, 2022.

[23] Qing Hua Wang, Kourosh Kalantar-Zadeh, Andras Kis, Jonathan N Coleman, and Michael S Strano. Electronics and optoelectronics of two-dimensional transition metal dichalcogenides. *Nature nanotechnology*, 7(11):699–712, 2012.

[24] KS Novoselov, Artem Mishchenko, Alexandra Carvalho, and AH Castro Neto. 2d materials and van der waals heterostructures. *Science*, 353(6298):aac9439, 2016.

[25] Jin-Wu Jiang. Graphene versus mos2: A short review. *Frontiers of Physics*, 10(3):287–302, 2015.

[26] Motohiko Ezawa. Photoinduced topological phase transition and a single dirac-cone state in silicene. *Physical review letters*, 110(2):026603, 2013.

[27] Hamid Oughaddou, Hanna Enriquez, Mohammed Rachid Tchalala, Handan Yildirim, Andrew J Mayne, Azzedine Bendounan, Gérald Dujardin, Mustapha Ait Ali, and Abdelkader Kara. Silicene, a promising new 2d material. *Progress in Surface Science*, 90(1):46–83, 2015.

[28] Jijun Zhao, Hongsheng Liu, Zhiming Yu, Ruge Quhe, Si Zhou, Yangyang Wang, Cheng Cheng Liu, Hongxia Zhong, Nannan Han, Jing Lu, et al. Rise of silicene: A competitive 2d material. *Progress in Materials Science*, 83:24–151, 2016.

[29] Deep Jariwala, Anchal Srivastava, and Pulickel M Ajayan. Graphene synthesis and band gap opening. *Journal of nanoscience and nanotechnology*, 11(8):6621–6641, 2011.

[30] MS Nevius, M Conrad, F Wang, A Celis, MN Nair, A Taleb-Ibrahimi, A Tejeda, and EH Conrad. Semiconducting graphene from highly ordered substrate interactions. *Physical review letters*, 115(13):136802, 2015.

[31] Dengyu Pan, Jingchun Zhang, Zhen Li, and Minghong Wu. Hydrothermal route for cutting graphene sheets into blue-luminescent graphene quantum dots. *Advanced materials*, 22(6):734–738, 2010.

[32] Si-Yu Li and Lin He. Recent progresses of quantum confinement in graphene quantum dots. *Frontiers of Physics*, 17:1–25, 2022.

[33] GY Wu, N-Y Lue, and L Chang. Graphene quantum dots for valley-based quantum computing: A feasibility study. *Physical Review B*, 84(19):195463, 2011.

[34] Tapash Chakraborty, Francois Peeters, and Uri Sivan. *Nano-Physics and Bio-Electronics: A New Odyssey*. Elsevier, 2002.

[35] RC Ashoori. Electrons in artificial atoms. *Nature*, 379(6564):413–419, 1996.

[36] Tapash Chakraborty. Quantum dots: A survey of the properties of artificial atoms. 1999.

[37] Stephanie M Reimann and Matti Manninen. Electronic structure of quantum dots. *Reviews of modern physics*, 74(4):1283, 2002.

[38] Theodore A Fulton and Gerald J Dolan. Observation of single-electron charging effects in small tunnel junctions. *Physical review letters*, 59(1):109, 1987.

[39] Leo Kouwenhoven and Leonid Glazman. Revival of the kondo effect. *Physics world*, 14(1):33, 2001.

[40] Yasuhiko Arakawa and Hiroyuki Sakaki. Multidimensional quantum well laser and temperature dependence of its threshold current. *Applied physics letters*, 40(11):939–941, 1982.

[41] Daniel Loss and David P DiVincenzo. Quantum computation with quantum dots. *Physical Review A*, 57(1):120, 1998.

[42] Xavier Michalet, Fabien F Pinaud, Laurent A Bentolila, James M Tsay, SJJL Doose,

Jack J Li, G Sundaresan, AM Wu, SS Gambhir, and S Weiss. Quantum dots for live cells, in vivo imaging, and diagnostics. *science*, 307(5709):538–544, 2005.

[43] Vediyappan Veeramani, Zhen Bao, Ming-Hsien Chan, Hung-Chia Wang, Anirudha Jena, Ho Chang, Shu-Fen Hu, and Ru-Shi Liu. Quantum dots for light conversion, therapeutic and energy storage applications. *Journal of Solid State Chemistry*, 270:71–84, 2019.

[44] Qianwen Liu, Jianhan Sun, Kun Gao, Nan Chen, Xiaotong Sun, Dan Ti, Congcong Bai, Ranran Cui, and Liangti Qu. Graphene quantum dots for energy storage and conversion: from fabrication to applications. *Materials Chemistry Frontiers*, 4(2):421–436, 2020.

[45] Michael Victor Berry and RJ Mondragon. Neutrino billiards: time-reversal symmetry-breaking without magnetic fields. *Proceedings of the Royal Society of London. A. Mathematical and Physical Sciences*, 412(1842):53–74, 1987.

[46] S Schnez, K Ensslin, M Sigrist, and T Ihn. Analytic model of the energy spectrum of a graphene quantum dot in a perpendicular magnetic field. *Physical Review B*, 78(19):195427, 2008.

[47] M Grujić, M Zarenia, A Chaves, M Tadić, GA Farias, and FM Peeters. Electronic and optical properties of a circular graphene quantum dot in a magnetic field: influence of the boundary conditions. *Physical Review B*, 84(20):205441, 2011.

[48] Morten Rishøj Thomsen and Thomas Garm Pedersen. Analytical dirac model of graphene rings, dots, and antidots in magnetic fields. *Physical Review B*, 95(23):235427, 2017.

[49] Ponomarenko LA Schedin F Katsnelson MI and R Yang. Hill ew novoselov ks geim ak

chaotic dirac billiard in graphene quantum dots. *Science*, 320:356, 2008.

[50] Jonathan Eroms and Dieter Weiss. Weak localization and transport gap in graphene antidot lattices. *New Journal of Physics*, 11(9):095021, 2009.

[51] Qiang Xu, Meng-Yue Wu, Grégory F Schneider, Lothar Houben, Sairam K Malladi, Cees Dekker, Emrah Yucelen, Rafal E Dunin-Borkowski, and Henny W Zandbergen. Controllable atomic scale patterning of freestanding monolayer graphene at elevated temperature. *ACS nano*, 7(2):1566–1572, 2013.

[52] AJM Giesbers, EC Peters, M Burghard, and K Kern. Charge transport gap in graphene antidot lattices. *Physical Review B*, 86(4):045445, 2012.

[53] Clyde Meador and AS Sarra. A comparison of two 4th-order numerical ordinary differential equation methods applied to the rabinovich–fabrikant equations. 2009.

[54] J De Frutos and JM Sanz-Serna. An easily implementable fourth-order method for the time integration of wave problems. *Journal of Computational Physics*, 103(1):160–168, 1992.

[55] William H Press. *Numerical recipes 3rd edition: The art of scientific computing*. Cambridge university press, 2007.

[56] Tomáš Harčarik, Jozef Bocko, and Kristína Maslákova. Frequency analysis of acoustic signal using the fast fourier transformation in matlab. *Procedia Engineering*, 48:199–204, 2012.

[57] DA Bahamon, ALC Pereira, and PA Schulz. Inner and outer edge states in graphene rings: A numerical investigation. *Physical Review B*, 79(12):125414, 2009.

[58] DR Da Costa, Andrey Chaves, M Zarenia, JM Pereira Jr, GA Farias, and FM Peeters. Geometry and edge effects on the energy levels of graphene quantum rings: A comparison between tight-binding and simplified dirac models. *Physical Review B*, 89(7):075418, 2014.

[59] Qiushi Zhang, Tsz Chun Wu, Guowen Kuang, Nian Lin, et al. Investigation of edge states in artificial graphene nano-flakes. *Journal of Physics: Condensed Matter*, 33(22):225003, 2021.

[60] Sharma SRKC Yamijala, Arkamita Bandyopadhyay, and Swapan K Pati. Structural stability, electronic, magnetic, and optical properties of rectangular graphene and boron nitride quantum dots: effects of size, substitution, and electric field. *The Journal of Physical Chemistry C*, 117(44):23295–23304, 2013.

[61] R Rieger and Klaus Müllen. Forever young: polycyclic aromatic hydrocarbons as model cases for structural and optical studies. *Journal of Physical Organic Chemistry*, 23(4):315–325, 2010.

[62] Alev Devrim Güçlü, Pawel Potasz, Marek Korkusinski, Pawel Hawrylak, et al. *Graphene quantum dots*. Springer, 2014.

[63] AD Güçlü, Pawel Potasz, and Pawel Hawrylak. Excitonic absorption in gate-controlled graphene quantum dots. *Physical Review B*, 82(15):155445, 2010.

[64] Ahmal Jawad Zafar, Aranyo Mitra, and Vadym Apalkov. Ultrafast valley polarization of graphene nanorings. *Physical Review B*, 106(15):155147, 2022.

[65] Tim Paasch-Colberg, Agustin Schiffrin, Nicholas Karpowicz, Stanislav Kruchinin,

Özge Sağlam, Sabine Keiber, Olga Razskazovskaya, Sascha Mühlbrandt, Ali Alnaser, Matthias Kübel, et al. Solid-state light-phase detector. *Nature Photonics*, 8(3):214–218, 2014.

[66] Jeffrey L Krause, Kenneth J Schafer, and Kenneth C Kulander. High-order harmonic generation from atoms and ions in the high intensity regime. *Physical Review Letters*, 68(24):3535, 1992.

[67] D Von der Linde, T Engers, G Jenke, P Agostini, G Grillon, E Nibbering, A Mysyrowicz, and A Antonetti. Generation of high-order harmonics from solid surfaces by intense femtosecond laser pulses. *Physical Review A*, 52(1):R25, 1995.

[68] PA Norreys, Matthew Zepf, S Moustaizis, AP Fews, Jianjun Zhang, P Lee, M Bakarezos, CN Danson, A Dyson, Paul Gibbon, et al. Efficient extreme uv harmonics generated from picosecond laser pulse interactions with solid targets. *Physical Review Letters*, 76(11):1832, 1996.

[69] Shambhu Ghimire, Anthony D DiChiara, Emily Sistrunk, Pierre Agostini, Louis F DiMauro, and David A Reis. Observation of high-order harmonic generation in a bulk crystal. *Nature physics*, 7(2):138–141, 2011.

[70] G Vampa, TJ Hammond, N Thiré, BE Schmidt, F Légaré, CR McDonald, T Brabec, and PB Corkum. Linking high harmonics from gases and solids. *Nature*, 522(7557):462–464, 2015.

[71] Georges Ndabashimiye, Shambhu Ghimire, Mengxi Wu, Dana A Browne, Kenneth J Schafer, Mette B Gaarde, and David A Reis. Solid-state harmonics beyond the atomic

limit. *Nature*, 534(7608):520–523, 2016.

[72] Hanzhe Liu, Yilei Li, Yong Sing You, Shambhu Ghimire, Tony F Heinz, and David A Reis. High-harmonic generation from an atomically thin semiconductor. *Nature Physics*, 13(3):262–265, 2017.

[73] Yong Sing You, Yanchun Yin, Yi Wu, Andrew Chew, Xiaoming Ren, Fengjiang Zhuang, Shima Gholam-Mirzaei, Michael Chini, Zenghu Chang, and Shambhu Ghimire. High-harmonic generation in amorphous solids. *Nature communications*, 8(1):724, 2017.

[74] Nicolai Klemke, Nicolas Tancogne-Dejean, Giulio M Rossi, Yudong Yang, F Scheiba, RE Mainz, G Di Sciacca, A Rubio, FX Kärtner, and OD Mücke. Polarization-state-resolved high-harmonic spectroscopy of solids. *Nature communications*, 10(1):1319, 2019.

[75] Nicolai Klemke, OD Mücke, Angel Rubio, Franz X Kärtner, and N Tancogne-Dejean. Role of intraband dynamics in the generation of circularly polarized high harmonics from solids. *Physical Review B*, 102(10):104308, 2020.

[76] Isak Kilen, Miroslav Kolesik, Jorg Hader, Jerome V Moloney, Ulrich Huttner, Maria K Hagen, and Stephan W Koch. Propagation induced dephasing in semiconductor high-harmonic generation. *Physical review letters*, 125(8):083901, 2020.

[77] Ferenc Krausz and Misha Ivanov. Attosecond physics. *Reviews of modern physics*, 81(1):163, 2009.

[78] Stanislav Yu Kruchinin, Ferenc Krausz, and Vladislav S Yakovlev. Colloquium: Strong-field phenomena in periodic systems. *Reviews of Modern Physics*, 90(2):021002, 2018.

[79] Agustin Schiffrin, Tim Paasch-Colberg, Nicholas Karpowicz, Vadym Apalkov, Daniel Gerster, Sascha Mühlbrandt, Michael Korbman, Joachim Reichert, Martin Schultze, Simon Holzner, et al. Optical-field-induced current in dielectrics. *Nature*, 493(7430):70–74, 2013.

[80] Jonas Kiemle, Philipp Zimmermann, Alexander W Holleitner, and Christoph Kastl. Light-field and spin-orbit-driven currents in van der waals materials. *Nanophotonics*, 9(9):2693–2708, 2020.

[81] Takuya Higuchi, Christian Heide, Konrad Ullmann, Heiko B Weber, and Peter Hommelhoff. Light-field-driven currents in graphene. *Nature*, 550(7675):224–228, 2017.

[82] Elisabeth Gruber, Richard A Wilhelm, Rémi Pétuya, Valerie Smejkal, Roland Kozubek, Anke Hierzenberger, Bernhard C Bayer, Inigo Aldazabal, Andrey K Kazansky, Florian Libisch, et al. Ultrafast electronic response of graphene to a strong and localized electric field. *Nature communications*, 7(1):13948, 2016.

[83] Shawn Sederberg, Dmitry Zimin, Sabine Keiber, Florian Siegrist, Michael S Wismer, Vladislav S Yakovlev, Isabella Floss, Christoph Lemell, Joachim Burgdörfer, Martin Schultze, et al. Attosecond optoelectronic field measurement in solids. *Nature communications*, 11(1):430, 2020.

[84] Giulio Vampa, Jian Lu, Yong Sing You, Denitsa R Baykusheva, Mengxi Wu, Hanzhe Liu, Kenneth J Schafer, Mette B Gaarde, David A Reis, and Shambhu Ghimire. Attosecond synchronization of extreme ultraviolet high harmonics from crystals. *Journal of Physics B: Atomic, Molecular and Optical Physics*, 53(14):144003, 2020.

[85] Maxim Trushin, Alexander Grupp, Giancarlo Soavi, Arne Budweg, Domenico De Fazio, Ugo Sassi, Antonio Lombardo, Andrea C Ferrari, Wolfgang Belzig, Alfred Leitenstorfer, et al. Ultrafast pseudospin dynamics in graphene. *Physical Review B*, 92(16):165429, 2015.

[86] Dong Sun, Jia-Wei Lai, Jun-Chao Ma, Qin-Sheng Wang, and Jing Liu. Review of ultrafast spectroscopy studies of valley carrier dynamics in two-dimensional semiconducting transition metal dichalcogenides. *Chinese Physics B*, 26(3):037801, 2017.

[87] Felice Gesuele. Ultrafast hyperspectral transient absorption spectroscopy: application to single layer graphene. In *Photonics*, volume 6, page 95. MDPI, 2019.

[88] Jun Zhang, Hao Ouyang, Xin Zheng, Jie You, Runze Chen, Tong Zhou, Yizhen Sui, Yu Liu, Tian Jiang, et al. Ultrafast saturable absorption of mos 2 nanosheets under different pulse-width excitation conditions. *Optics Letters*, 43(2):243–246, 2018.

[89] D Golde, T Meier, and Stephan W Koch. High harmonics generated in semiconductor nanostructures by the coupled dynamics of optical inter-and intraband excitations. *Physical Review B*, 77(7):075330, 2008.

[90] Suresh Gnawali, Rupesh Ghimire, Krishna Rana Magar, Sayed Jaber Hossaini, and Vadym Apalkov. Ultrafast electron dynamics of graphene quantum dots: High harmonic generation. *Physical Review B*, 106(7):075149, 2022.